J. Fluid Mech. (1999), *vol.* 382, *pp.* 155–193. Printed in the United Kingdom

Dynamics of corotating vortex pairs in the wakes of flapped airfoils

By A. L. CHEN, J. D. JACOB AND Ö. SAVAŞ

Department of Mechanical Engineering, University of California at Berkeley, Berkeley, CA 94720-1740, USA
e-mail: savas@me.berkeley.edu

(Received 12 December 1997 and in revised form 20 August 1998)

The behaviour of a pair of corotating vortices in the wake of a flapped airfoil is experimentally studied in a water towing tank. Reynolds numbers based on total circulation of the vortices range from 1.0×10^4 to 6.4×10^4. Planar velocity vector fields and their gradients are derived from PIV images using an adaptive Lagrangian parcel tracking algorithm. Isovorticity surfaces are extracted from time series of planar vorticity data. The behaviour of the vortices is tracked by using various moments of both the probability density distribution and the spatial distribution of their streamwise vorticity. All vortices show a Lamb–Oseen circulation distribution when they are clearly identifiable. Further, vortices from the flapless wing exhibit Lamb–Oseen velocity and vorticity distributions with slow growth. All corotating vortex pairs are observed to merge at about 0.8 orbit periods. First-order statistics of the flow field remain invariant during the merger. The higher-order moments of the vorticity distribution show strong time dependence, which implies three-dimensionality of the flow resulting from vortex stretching. The strengths of the individual vortices before merger are constant, and the total circulation before and after merger remains constant within the range of observations. The trajectory of the centre of vorticity remains unaffected by the merger process. The merger is preceded by a splitting of the weaker vortex into filaments which, depending on the relative strengths of the vortices, can occur in the radial direction, the axial direction, or a combination of the two. Mechanisms contributing to the merger dynamics are discussed.

1. Introduction

A counter-rotating vortex system is present in the wake of any finite lifting wing. This vortex system poses a safety problem in air transport which manifests itself directly as aircraft–vortex encounters with a wide range of consequences, and indirectly as one of the primary factors in scheduling take-offs and landings at airports. The current approach to this problem consists of attempts to avoid the wake vortices in air operations which is becoming increasingly difficult. An alternative approach is either eliminating the vortex wake completely or mitigating the danger posed by it. Both of these require an understanding of the basic dynamics of the wake vortex system, which is currently inadequate.

Current experience is almost exclusively based on two-dimensional arguments and limited to restricted experiments. The efforts hitherto have been cyclical with a flurry of activity over a few years which wanes once the problem has been determined unsolvable with the current level of understanding of the flow physics and the

available technology. Some of the important gatherings dedicated to the topic include the Symposium on Aircraft Wake Turbulence and its Detection (Olsen, Goldberg & Rogers 1971), Symposium for Wake Vortex Minimization (Gessow 1976), FAA International Wake Vortex Symposium (FAA 1991), NATO-AGARD Symposium on Wakes from Lifting Vehicles (AGARD 1996), and a comprehensive Wake Vortex Bibliography (Hallock 1991*a*, *b*, 1997). In addition, several technical programs have been created to address this problem (Balser, McNary & Nagy 1974; Kopp 1994), notably the Aircraft Vortex Spacing System (AVOSS) (Hinton 1996) which is currently being examined for implementation. These still rely on accurate predictive capabilities of vortex behaviour, which are limited at this time.

The formation of the vortex wake behind a finite wing has received specific attention. The process was first conceptually proposed by Lanchester (1908) at the turn of the century. The basic theory of vortex wake formation was not well codified until the 1950s (Spreiter & Sacks 1951), however, and not until the 1970s did trailing vortex stability and breakdown begin to receive adequate treatment (Crow 1970; Maxworthy 1972; Hall 1972; Moore & Saffman 1973, 1975; Tsai & Widnall 1976). At this stage, theory was well ahead of both numerical and experimental investigation, as witnessed by the research at the time (Olsen *et al*. 1971; Gessow 1976). Twenty years later, the latter elements have begun to reach the level of reliability and sophistication of the former. On the numerical side, two-dimensional simulations have been the norm due to their reduced computing costs. The obvious question arises whether these results can be extrapolated to three dimensions (Spalart 1998). This question is slowly fading as simulations become more and more robust and are able to handle more complex geometry. Still, the accurate simulation of a full-scale aircraft wake at the required Reynolds numbers is distant. Current simulations are essential in examining the importance of three-dimensional effects on single or multiple periodic vortex systems, though, such as short-wave or long-wave instabilities. On the experimental side, the advent of non-intrusive field techniques has greatly improved the amount of data. The main benefit is the ability to examine the instantaneous (i.e. unsteady) behaviour of a vortex system (Jacob, Savaş & Liepmann 1997). In addition, traditional laboratory and field-test techniques continue to make contributions. For example, recent hot-wire probe measurements in a wind tunnel have shown that corotating vortices merge into a single vortex with significantly different turbulence characteristics (Vogel, Devenport & Zsoldos 1996). Full-scale tests have been conducted which have the benefit of including all of the requisite physics, but whose benefits are often outweighed by the cost of the experimental runs and the limited quality of the data (e.g. Garodz & Clawson 1993).

Recent work has also shown that trailing vortices can be altered to some degree by various means (Croom 1976; Greene 1986; Rossow *et al*. 1995; Jacob, Liepmann & Savaş 1996; Crouch 1997), including methods which use merger for mitigation. Whether the alterations can significantly impact a full-scale wake to the magnitude required is still in question, though. More specifically, disagreement exists over the details of the physics behind alleviation attempts, and even whether any alleviation is at all possible. This is due in large part to the number of parameters in vortex formation and evolution.

The goal of this study is to contribute to the understanding of the dynamics of a corotating vortex pair in a vortex wake. The prevailing view is that a corotating vortex pair in the wake of a flapped airfoil may be treated as a two-dimensional system, which should not merge unless the vortex cores are sufficiently large, where straining would result in merger (Spalart 1998). Laboratory experiments at sufficiently

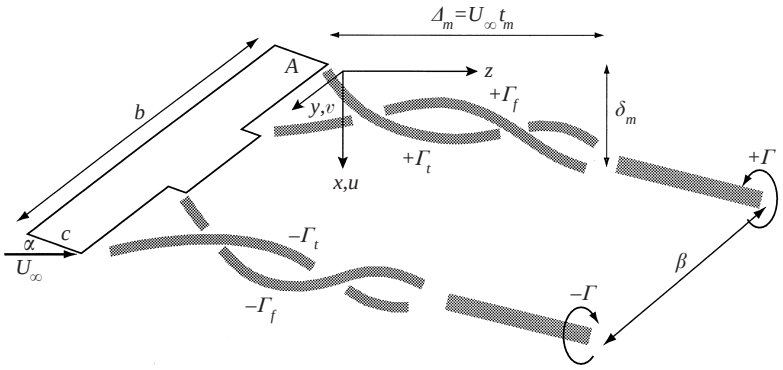

FIGURE 1. Sketch defining the vortex wake problem and the left-handed x, y, z-coordinate system.

high Reynolds numbers have shown little interaction between such vortices, leading to the belief that the vortices will retain their identities and will not merge for a long time (de Bruin *et al*. 1996). However, in these experiments, the downstream distances at which measurements are made are typically limited to a fraction of the orbit time of the vortex system; hence, the measurements have not fully captured the dynamics of the vortices. Studies beyond the near field of the wing have shown significant interaction between the vortices of single or multiple vortex pairs (P. S. Marcus & T. Matsushima 1995, personal communication; Vogel *et al*. 1996; Jacob *et al*. 1997).

The flow considered here is the interaction of corotating vortices in the wake of a finite lifting wing with flaps. The flow configuration and the reference system are shown in figure 1. The wing has a span of b, a chord c, and an area A, with the edges of a continuous flap at a distance of l away from the wing tips. It is at an angle of attack of α and is moving at a velocity of U_∞. A corotating vortex pair is generated off each side of the wing with strength of $\pm\Gamma_t$ from the wing tips and $\pm\Gamma_f$ from the flap tips. For high aspect ratio wings with small l/b, the corotating vortex system displays internal behaviour independent of the vortex system shed off of the other half of the wing. The internal dynamics of the corotating system lead to single vortices of strength $\pm\Gamma$ which form the conventional counter-rotating vortex pair of the far wake. The merger of the $\pm\Gamma_t$ and $\pm\Gamma_f$ vortices occurs at some downstream distance $\Delta_m = U_\infty t_m$, where t_m is the time to the merger. By the merger time, the counter-rotating vortex system descends a distance of δ_m where the $\pm\Gamma$ vortices are separated by a distance β. The interesting flow details become detectable after about 1/4 orbit time, and the prominent dynamics are observed within one orbit time. The events in the wake take place on the time scale of the orbiting period of the corotating pair. This time scale dictates the vortex descent and downstream distance to merger. The merger descent distance δ_m is found to be independent of the flow conditions while Δ_m is too long to be observed in a typical wind tunnel.

The experimental setup and the data processing are described first. Following that is a qualitative description of sample flows, which is based on the vorticity fields. Next is a detailed discussion of the sample flows with emphasis on structure, kinematics, and dynamics of the vortices. Lastly, merger dynamics are discussed and the findings of the paper are summarized.

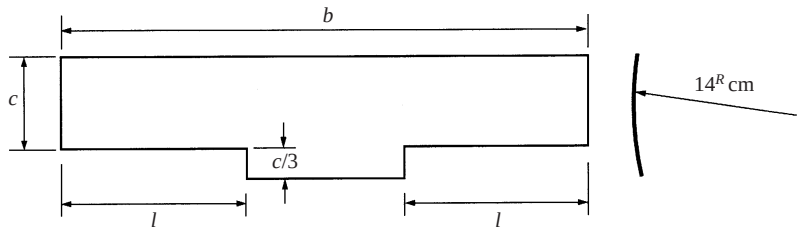

FIGURE 2. Wing geometry showing plan view, circular profile, and dimension definitions.

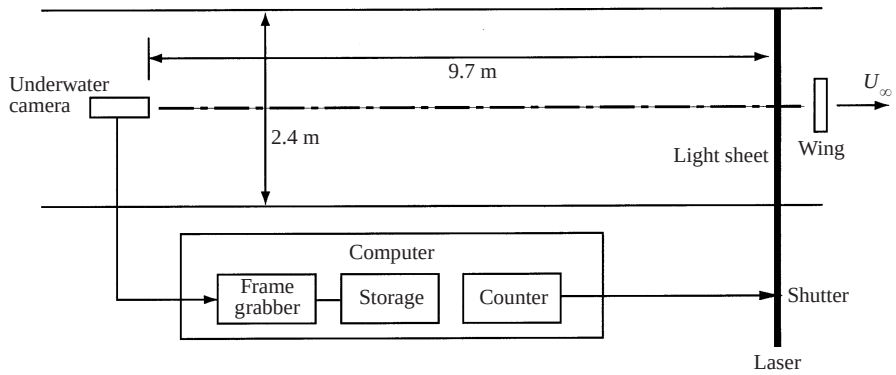

FIGURE 3. Experimental setup showing tow tank, wing, camera, light sheet, and data acquisition computer.

2. Experimental setup

2.1. *Airfoil geometry*

The airfoils are of a rectangular planform with a circular arc profile of 14 cm radius and constructed of 1.1 mm thick stainless steel (figure 2). The curvature is intended for improved wing performance at low Reynolds numbers. The airfoils have a span of $b = 30.5$ cm and a chord length of $c = 5.1$ cm, resulting in an aspect ratio of 6. Step changes in lift distribution are obtained with flap extensions beyond the trailing edge. Two flap spans are used: 30% ($l = 10.7$ cm) and 67% ($l = 5.0$ cm). In addition, measurements are made with an unflapped wing for comparison. The airfoil is attached to a towing carriage by a strut mounted on the airfoil centreline. The strut to the carriage is a thin flat plate with a chord length of 2.5 cm, a thickness of 3.2 mm, and faired leading and trailing edges. The angle of attack α of the airfoils is varied from 0° to $+8^\circ$ in 2° increments.

2.2. *Flow apparatus*

The experiments were conducted in the University of California–Berkeley water towing tank facility shown in figure 3. The tank is approximately 70 m long and 2.4 m across with a nominal depth of 1.7 m. The towing speed U_∞ is variable from 10 to 160 cm s^{-1} at an accuracy of better than 1%. The tank has a viewing station near the centre of the length of the tank consisting of a 3 m long window. The water temperature is approximately 18 °C (kinematic viscosity $\nu = 0.01$ cm^2 s^{-1}). A 5 mm thick light sheet from a 10 W CW laser is projected normal to the tow velocity through the viewing window. The immediate vicinity of the light sheet is seeded with 40 μm silver-coated hollow glass spheres. Any motion of the water induced by the

seeding mechanism is allowed to damp out before an experimental run takes place. A camera is placed underwater at a 90° viewing angle to the light sheet and centred at a distance of 9.7 m behind the sheet. The camera (Sony XC-7500) is a 30 Hz progressive-scan analogue monochrome non-interlaced charge-coupled device (CCD) with a 640×480 square pixel chip. A 75–200 mm zoom lens (Canon 1:4.5 FD) is attached to the camera. To increase the spatial resolution of the measurements, only half of the wake of the airfoil is imaged. The imaged area is about 40×30 cm. A mechanical shutter synchronized with the camera is placed in front of the laser to reduce image streaking. The resulting images are stored in real time in memory on a computer using an imaging board (Matrox Pulsar) and then written to disk. In an experimental run, the wing starts its motion immediately in front of the camera. Data acquisition starts as soon as the wing arrives at the laser sheet. The wing continues its motion uninterrupted until the data acquisition is complete. Seven to ten seconds of data are recorded during each experimental run. Data are taken at downstream distances up to $z/b = 52$ ($z/c = 314$).

2.3. *Data processing*

A modified version of the Lagrangian parcel tracking (LPT) algorithm developed by Sholl & Savaş (1997) is used for particle image velocimetry (PIV) processing. The algorithm treats the seeding particles as markers of fluid parcels and tracks both their translations and deformations. The velocity field needed to initialize the LPT process is obtained from a conventional PIV algorithm which uses multiple passes, interrogation window shifting, and adjustable interrogation window size. Both the LPT and PIV algorithms employ a rigorous peak-detection scheme to determine velocity vectors, and use the local velocity gradient tensor to identify spurious velocity vectors. The LPT algorithm works well in the flow field of a vortex, which is characterized by high deformations and where traditional PIV algorithms are plagued by biasing and limited dynamic range. Finer resolution of the velocity vector field is obtained with an adaptive LPT algorithm (aLPT). Based on the magnitude and the direction of the expected velocity vector determined from a previous LPT pass, the size (small or large), shape (square or rectangular), and orientation (horizontal or vertical rectangles) of the interrogation window are adjusted to maximize correlation information and to minimize calculation time. The output of the algorithm consists of the velocity vector (u, v) and its gradient tensor

$$u_{ij} = \begin{pmatrix} \partial u/\partial x & \partial u/\partial y \\ \partial v/\partial x & \partial v/\partial y \end{pmatrix} \tag{2.1}$$

at each point, from which the axial vorticity $\omega = (\partial v/\partial x - \partial u/\partial y)$ is determined in the plane of measurement. The u_{ij} tensor is an intrinsic product of the algorithm and is calculated spectrally. Post-processing is performed with Research Systems Interactive Data Language (IDL).

Sample data are shown in figure 4. Figure 4(*a*) shows one frame of a pair of images used in the aLPT processing. The streaklines make visible the tip and flap vortices which have rotated about 180° from their initial orientation. The image shows typical problems plaguing PIV algorithms such as uneven seeding density, local saturation, local darkness, and excessive streaking. The aLPT algorithm is able to derive velocity information from the images without difficulty. The velocity vector field (u, v) and selected streamlines corresponding to the image in figure 4(*a*) are shown in figure 4(*b*). The axial vorticity field $\omega(x, y)$ is shown in figure 4(*c*). The (u, v) and ω arrays are 73 (vertical) × 53 (horizontal) in size. The overlap of the

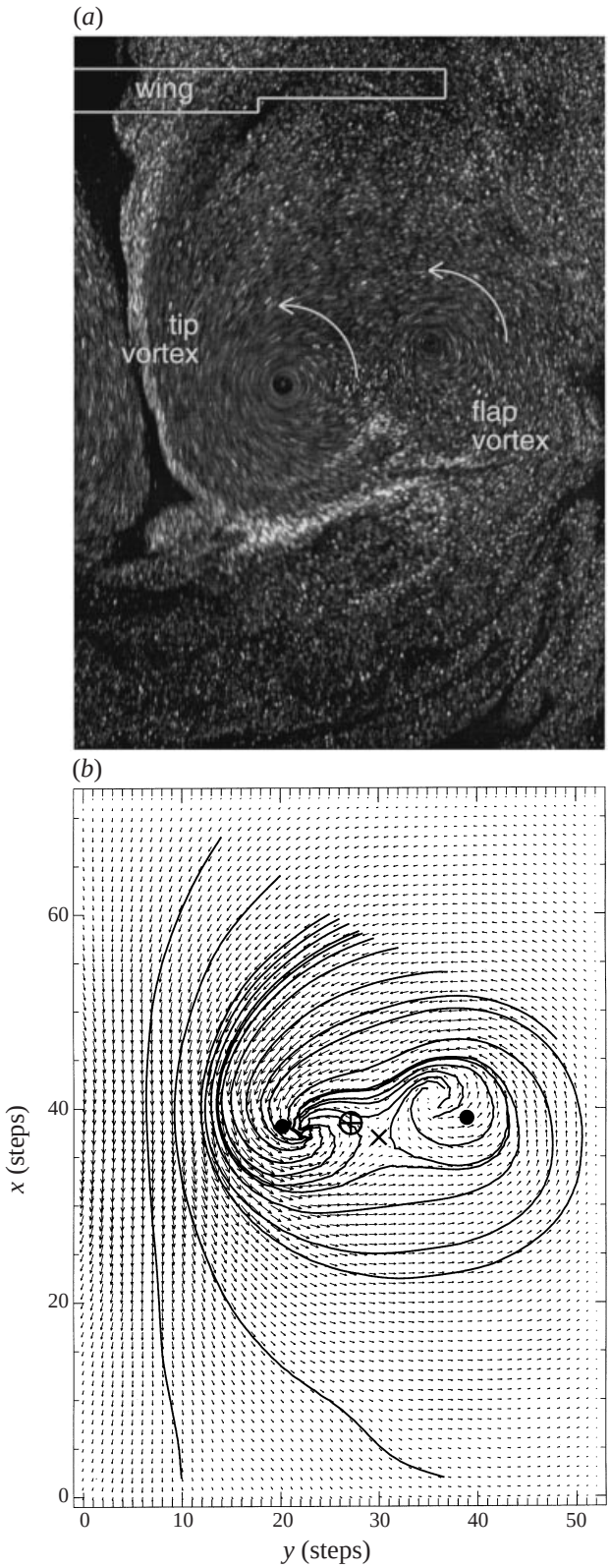

FIGURE 4 (*a, b*). For caption see facing page.

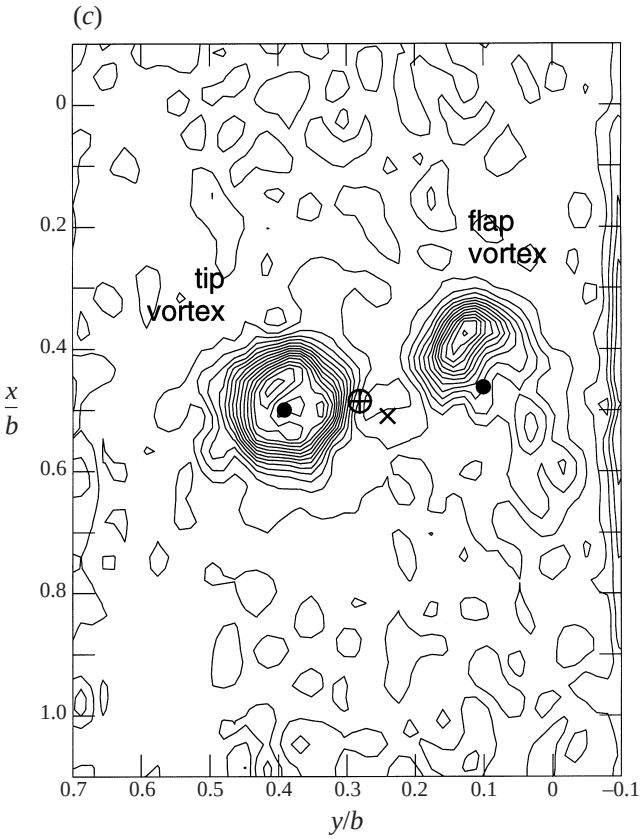

FIGURE 4. Sample PIV image and aLPT results from flow 16 in table 1. (*a*) Photograph showing vortex pair, streaks, and non-uniform seeding 5 s after the 30% flap wing passed by at $U_\infty = 160$ cm/s. Note that the vortices have rotated about 180° from their initial orientation (see figure 7 below). (*b*) Cross-plane velocity vector plot from aLPT (73 × 53) and the corresponding streamline pattern. (*c*) Vorticity contours from aLPT: ●, centres of vorticity for the flap and the tip vortices; ⊕, centre of vorticity of the vortex pair, and ×, common stagnation point of the pair.

corresponding correlation windows during the aLPT processing ranges from 0 to 50%. These streamlines are in the laboratory reference frame and are substantially different from the streakline pattern seen in (*a*). The vectors in figure 4(*b*) indicate three stagnation points, one corresponding to each of the vortices and one to the centroid of vorticity. The stagnation points corresponding to the individual vortices are at the ends of spiralling streamlines, and that corresponding to the combined system is near the centroid of vorticity of the pair. The far-field streamline pattern indicates a descending patch of vorticity into which the flow spirals. The stronger vortex acts as an attractor of the streamlines of the whole system. In identifying the locations of the individual vortices and the centroid, the vorticity field provides the most rigorous information. The markers in figure 4(*b*) are determined from the vorticity data in figure 4(*c*). In this particular calculation, the vortices are visually bracketed in the largest non-overlapping rectangular regions, the edges of which are in nominally zero-vorticity regions. The centre of the total vorticity distribution is that of the two rectangular regions used for the individual vortices. In figure 4(*c*), the marker identifying the centre of the tip vortex is nearly at the centre of the vorticity

contour lines, which shows a compact vorticity distribution. The marker identifying the flap vortex is substantially displaced from the peak vorticity. This is attributed to the fact that the flap vortex is undergoing a splitting mechanism which precedes the merger of these two vortices. This is due to the splitting of the vortex which spreads vorticity over the 'tail' of the vortex. The centres of the vortices are displaced from the two stagnation points due to the orbiting motion of the vortices. Similarly, the centroid is at a different location from the common stagnation point in figure 4(*b*).

3. Discussion of results

3.1. *General observations*

The flows listed in table 1 form the basis of this paper. The wing planform, the towing speed U_∞, and the angle of attack α are the controlled parameters of the flows. The measured parameters are the total circulation $\Gamma = \Gamma_t + \Gamma_f$, the circulation ratio Γ_f/Γ_t, the counter-rotating vortex separation distance β, vortex size parameters σ_t and σ_f (defined below), the merger time t_m, and the descent distance to merger δ_m. The chord Reynolds number $Re_c = cU_\infty/\nu$ ranges from 4.1×10^4 and 8.2×10^4 and the circulation Reynolds number $Re_\Gamma = \Gamma/\nu$ from 1.0×10^4 to 6.4×10^4. Flow measurements are first presented as isovorticity surfaces, abbreviated as *isovor*(*s*) hereafter. These surfaces are extracted from three-dimensional data sets of the axial vorticity component, which are constructed from time series of planar data. A complete set of the isovors are presented in Chen, Jacob & Savaş (1997). The isovors depict the behaviour of a single vortex in figure 5, the rapid merger of two close vortices at low Reynolds numbers in figure 6, and the merger of widely separated vortices with various circulation ratios in figures 7 and 8. The multi-dimensional data alleviate uncertainties due to the wandering of vortices when single-point measurements are made. Even though the effect of wandering on average quantities may be corrected by deconvolution (Baker *et al*. 1974; Devenport *et al*. 1996), the details of the flows are lost.

Several interesting observations of vortex characteristics, their interaction, and merger can be made from the isovors. First, the events in the figures are at sufficiently high Reynolds numbers that the vortex dynamics are inertia-dominated. Vortex pairs initially have separations of either 5 cm or 10 cm and merge in a distance on the order of 10 m. The elapsed time t is converted to distance through the towing velocity as tU_∞. An experimental run typically lasts 10 s, during which time the viscous diffusion length is $(\nu t)^{1/2} \sim 3$ mm ($\sim 0.01b$). The spatial resolution of aLPT in the figures is about 3 mm. Hence, the resolved length scale cannot differentiate diffusive events on the basis of individual measurements. Averaged measurements, however, can yield clues about viscous diffusion as discussed below in conjunction with the growth of vortices. A guideline in identifying flow features is to confirm that they are not confined to a single plane of data, but can be traced in time over many frames. Figures 7 and 8 show consistent details at low vorticity levels which persist throughout the flows. In addition, the flow images that are used in aLPT processing are also used as flow visualization pictures in interpreting the results during the data analysis (see figure 4(*a*)), which proved to be of extreme value in confirming and interpreting the features revealed by the isovors.

3.2. *Flow details*

Figure 5 shows isovors in the wake of the unflapped wing at $\alpha = 4^\circ$ and $U_\infty = 160$ cm s^{-1} (flow 4; $Re_c = 8.2\times10^4$, $Re_\Gamma = 2.4\times10^4$). The vortex sheet off the wing rapidly rolls up into a single vortex which moves inboard and descends under the induced

flow #	% flap	U_∞ (cm s^{-1})	α (deg.)	Γ (cm^2 s^{-1})	Re_Γ (Γ/ν)	Γ_f/Γ_t	β (cm)	σ_t (cm)	σ_f (cm)	t_m (s)	δ_m (cm)
1	0	80	8	170	17 000	—	24.6	1.9	—	—	—
2	0	160	0	100	10 000	—	35.6	1.8	—	—	—
3	0	160	2	150	15 000	—	20.7	1.9	—	—	—
4	0	160	4	240	24 000	—	28.2	2.1	—	—	—
5	0	160	6	360	36 000	—	26.2	2.3	—	—	—
6	0	160	8	340	34 000	—	26.7	2.5	—	—	—
7	30	80	0	170	17 000	1.30	28.5	1.8	2.0	27.0	26.7
8	30	80	4	200	20 000	0.75	27.2	2.0	1.9	18.0	22.9
9	30	80	4	260	26 000	0.78	24.1	1.9	2.3	14.7	24.4
10	30	80	6	280	28 000	0.47	25.6	2.1	1.8	19.0	32.9
11	30	80	8	250	25 000	0.51	19.6	1.8	2.1	17.0	35.4
12	30	160	0	300	30 000	1.02	22.1	2.3	2.0	12.0	24.0
13	30	160	2	360	36 000	1.01	22.4	2.0	2.0	13.0	33.7
14	30	160	4	420	42 000	0.46	24.4	2.0	1.6	10.0	27.9
*15	30	160	4	480	48 000	0.57	26	2.8	2.1	7.0	22
16	30	160	4	540	54 000	0.61	24.6	2.5	2.7	7.7	28.0
17	30	160	4	430	43 000	0.50	23.7	2.4	2.1	8.5	23.6
18	30	160	4	550	55 000	0.58	23.2	2.5	2.2	8.7	32.8
19	30	160	6	600	60 000	0.44	24.2	2.5	2.5	6.7	26.1
20	30	160	8	450	45 000	0.46	25.5	2.1	1.9	6.0	16.1
21	30	160	8	500	50 000	0.40	18.2	2.1	1.5	6.0	23.5
22	30	160	8	520	52 000	0.32	20.0	2.1	1.9	6.0	22.2
23	30	160	8	500	50 000	0.47	24.4	2.9	2.7	6.4	22.1
24	67	80	0	150	15 000	0.95	21.0	1.1	1.2	4.9	6.6
25	67	80	2	190	19 000	0.77	26.7	1.0	1.2	4.5	6.2
26	67	80	4	240	24 000	0.67	26.0	1.0	1.2	3.3	5.2
27	67	80	4	260	26 000	0.67	25.4	1.2	1.3	2.6	4.3
28	67	80	8	290	29 000	0.70	23.0	1.2	0.9	2.1	4.5
29	67	80	8	290	29 000	0.65	19.3	1.3	0.8	2.4	6.2
30	67	160	0	350	35 000	1.20	22.8	1.1	1.2	1.7	4.4
31	67	160	0	350	35 000	1.30	23.2	1.2	1.3	2.0	5.1
32	67	160	2	480	48 000	1.30	21.6	1.3	1.3	1.5	5.3
33	67	160	4	540	54 000	0.65	21.7	1.6	1.1	1.6	6.2
34	67	160	4	540	54 000	0.73	23.2	1.5	1.2	1.3	4.7
35	67	160	4	540	54 000	0.85	22.1	1.5	1.4	1.2	4.7
36	67	160	8	620	62 000	0.40	20.5	1.9†	—	0.9	4.4
37	67	160	8	620	62 000	0.49	21.4	2.0†	—	1.2	5.6
38	67	160	8	605	60 500	0.40	21.8	2.0†	—	1.3	5.7
39	67	160	8	640	64 000	0.40	21.0	2.1†	—	1.1	5.4

*Anomalous flow. † Merged vortex size.

TABLE 1. Schedule of experiments and some measured quantities.

flow field of its companion vortex off the other end of the wing. The vortex assumes a circular shape rapidly after roll up and preserves this shape during the measurement period. All surface levels show similar behaviour: a coherent vortex which descends uneventfully. The vortex in figure 5 shows little growth except when very close to the wing. The growth in size is especially evident for the higher value isovors and is confined to about $z/b < 5$ ($z/c < 30$). This growth is partially due to the roll-up of the vortex sheet and is in good agreement with predictions of roll-up completion distance (Spreiter & Sacks 1951; Crow 1970; Saffman 1992). No obvious signs of instabilities

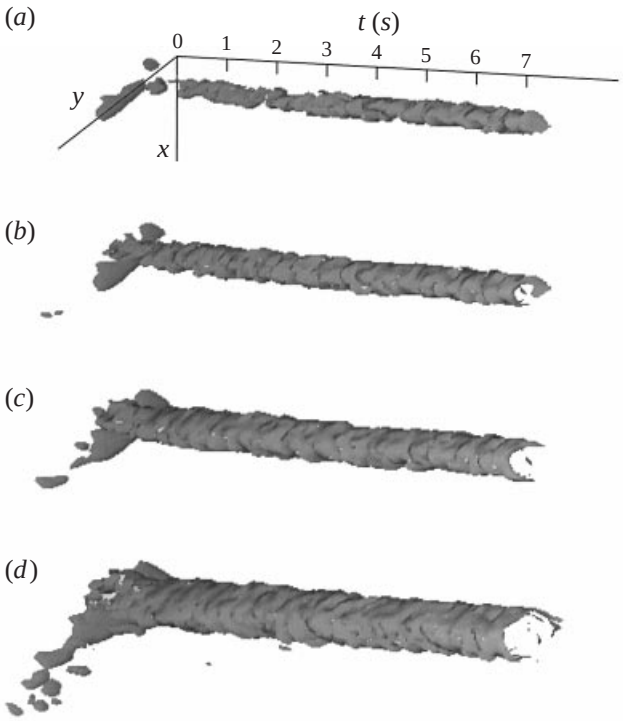

FIGURE 5. Flow 4. Isovors showing the behaviour of the core and peripheral vorticity distribution of a single descending vortex. Wing without flap at $\alpha = 4^\circ$ angle of attack and $U_\infty = 160$ cm/s towing speed. (*a*) $\omega = 12.0$ s^{-1}, (*b*) $\omega = 9.0$ s^{-1}, (*c*) $\omega = 6.0$ s^{-1}, and (*d*) $\omega = 3.0$ s^{-1}.

are apparent, though the sampling rate precludes the possibility of observing short-wave instabilities. Some of the details on the surface on the isovors are due to the inherent noise resulting from the data analysis; some may be indicative of instabilities or stretching of the vortex.

Figure 6 shows isovors in the wake of the wing with a 67% flap at $\alpha = 0^\circ$ and $U_\infty = 80$ cm s^{-1} (flow 24; $Re_c = 4.1 \times 10^4$, $Re_\Gamma = 1.8 \times 10^4$). These low-speed data are presented to highlight the vortex merger which would have occurred sooner at higher angles of attack and higher towing speeds. In addition, the figure shows a vortex pair with one of the lowest Re_Γ where the viscous effects are expected to be at their highest. Initially, the tip vortex moves partially up out of view while the flap vortex is descending (also in figures 7 and 8 below). After the tip vortex comes into view, the orbiting motion of the pair is clearly observable. The individual vortices and the merged vortex in this flow have much smaller circulations than the vortex in figure 5, as is clear from the smaller cross-sections of the same level of the isovors in figure 6. The cores remain separate for a long period of time. The pair orbit around each other as they descend, and early signs of interaction between them are apparent. The tip vortex dominates the flow, while the flap vortex shrinks and loses its identity in the flow field of the stronger tip vortex. Flutes develop on the weaker flap vortex. The merger appears to have occurred by the time the vortices complete one orbit. After the merger, the core of the system straightens immediately (figure 6*c*) and proceeds to descend much like the single vortex in figure 5. Again, as remarked in the discussion of figure 5, the merged vortex does not show any significant growth. Similar behaviour is observed in the final vortex when the merger occurs close to

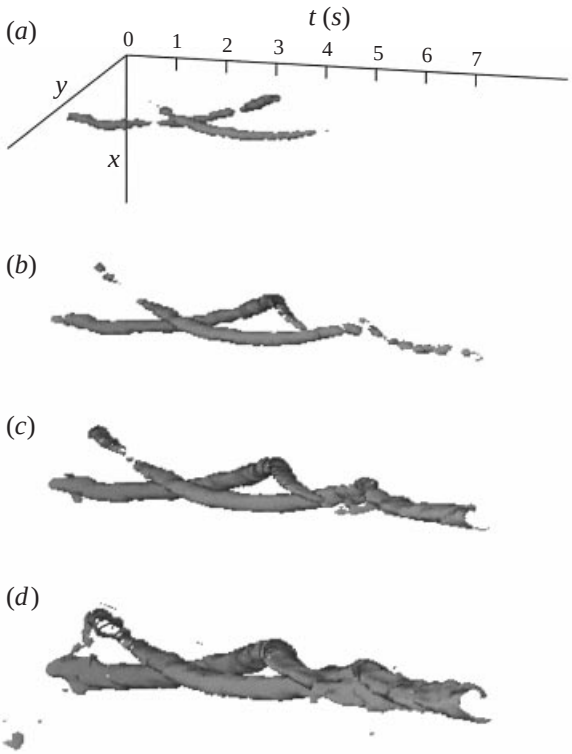

FIGURE 6. Flow 24. Isovors showing the behaviour of the core and peripheral vorticity distribution of a corotating vortex pair at small separation and low speed. 67% flap wing at $\alpha = 0^\circ$ and $U_\infty = 80$ cm/s towing speed. (*a*) $\omega = 15.0$ s^{-1}, (*b*) $\omega = 12$ s^{-1}, (*c*) $\omega = 9.0$ s^{-1}, and (*d*) $\omega = 6.0$ s^{-1}.

the wing at higher angles of attack (flows 24–39, table 1). Both vortices show signs of undulations on their surfaces. Further, the vortices, especially the flap vortex, are clearly unable to maintain a circular shape. These may be indicators of long-wave vortex instabilities, core oscillations, and vortex stretching.

Figure 7 shows isovors in the wake of the wing with a 30% flap at $\alpha = 4^\circ$ and $U_\infty = 160$ cm s^{-1} (flow 16, $Re_c = 8.2 \times 10^4$). The Reynolds number for the tip vortex is $Re_{\Gamma,t} = 3.0 \times 10^4$ and for the flap vortex $Re_{\Gamma,f} = 2.5 \times 10^4$. Flow separation over the centre portion of the wing causes loss of lift, thereby weakening the flap vortex. The tip vortex is now the dominant one. The vortices merge within the view, and the merger is completed within one orbit time as observed in figure 6. In contrast, however, the vortices here are at a Reynolds number nearly an order of magnitude higher. In addition, the merger is clearly an inviscid process as evidenced by the lack of any smooth 'bridges' between the vortices at vorticity levels above the background noise. The weaker flap vortex experiences an instability mechanism which splits it into streamwise filaments. This splitting seems to occur in the axial direction for this flow. Of these filaments, some merge with the dominant tip vortex right away, some continue orbiting and merge at a later time, and yet others shrink and redistribute their vorticity around the core. The weaker flap vortex follows a helix with a higher pitch angle than that followed by the stronger tip vortex. After the merger of the two vortices, the trajectory of the core of the system becomes straight almost instantaneously.

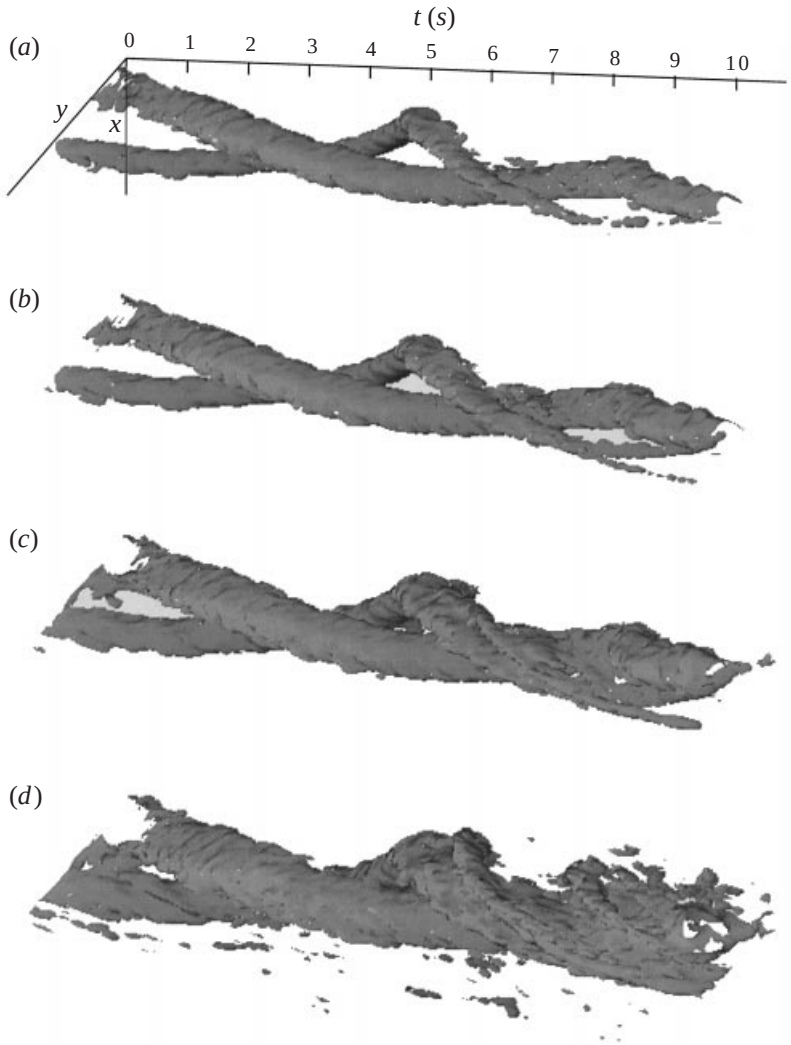

FIGURE 7. Flow 16. Isovors showing the behaviour of the core and peripheral vorticity distribution of a corotating vortex pair at large separation and moderate angle of attack. 30% flap wing at $\alpha = 4^\circ$ and $U_\infty = 160$ cm/s towing speed. (*a*) $\omega = 6.0\ \mathrm{s}^{-1}$, (*b*) $\omega = 4.5\ \mathrm{s}^{-1}$, (*c*) $\omega = 3.0\ \mathrm{s}^{-1}$, and (*d*) $\omega = 1.5\ \mathrm{s}^{-1}$.

Figure 8 shows isovors in the wake of the wing with a 30% flap at $\alpha = 8^\circ$ and $U_\infty = 160$ cm s^{-1} (flow 23; $Re_c = 8.2 \times 10^4$). The Reynolds number for the tip vortex is $Re_{\Gamma,t} = 3.3 \times 10^4$ and for the flap vortex $Re_{\Gamma,f} = 2.2 \times 10^4$. The figure shows a flow with a fairly high Reynolds number. Due to the higher angle of attack, strong separation has occurred that substantially weakens the flap vortex, which is much weaker than the tip vortex. Therefore, the interaction here is between two disparate vortices at a high circulation Reynolds number, which brings additional interesting features into the interaction picture. The flap vortex orbits on a large circle, while the tip vortex follows a smaller orbit. The merger seems to occur sooner and is again marked by a sudden transition of the core trajectory from a helix to a straight line. A more interesting observation is, however, the formation of the fine filament

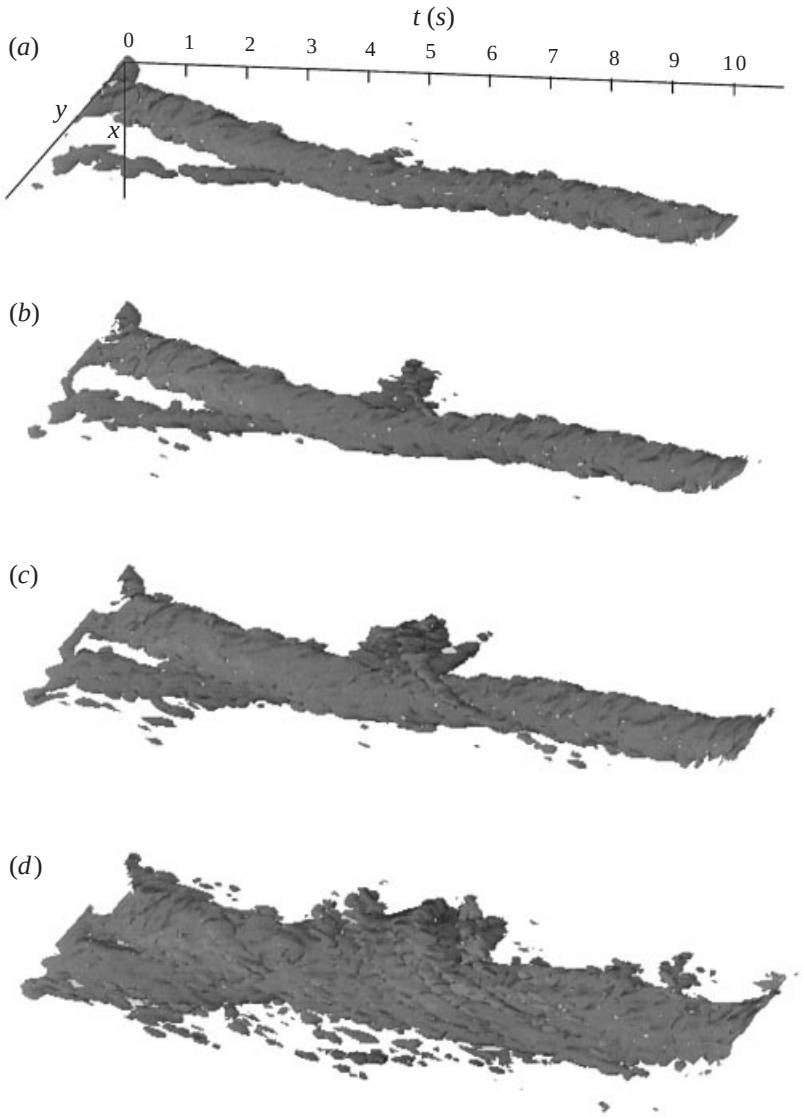

FIGURE 8. Flow 23. Isovors showing the behaviour of the core and peripheral vorticity distribution of a corotating vortex pair at large separation and high angle of attack. 30% flap wing at $\alpha = 8^\circ$ and $U_\infty = 160$ cm/s towing speed. (*a*) $\omega = 6.0$ s^{-1}, (*b*) $\omega = 4.5$ s^{-1}, (*c*) $\omega = 3.0$ s^{-1}, and (*d*) $\omega = 1.5$ s^{-1}.

structure of the flap vortex and the manner in which this occurs. First the flap vortex destabilizes and splits radially. The weaker filaments hurled into the orbit of the tip vortex start circling on lower pitch trajectories as they shrink and redistribute vorticity around the perimeter. The stronger inner filaments, on the other hand, seem to merge with the vortex core rapidly. Signs of instabilities are apparent on the cores, especially on the flap vortex.

3.3. *Summary of flows*

The flows presented in figures 5–8 suggest that the dynamics of the corotating vortices in the wake depend strongly on their strengths, separation, and core sizes. The details

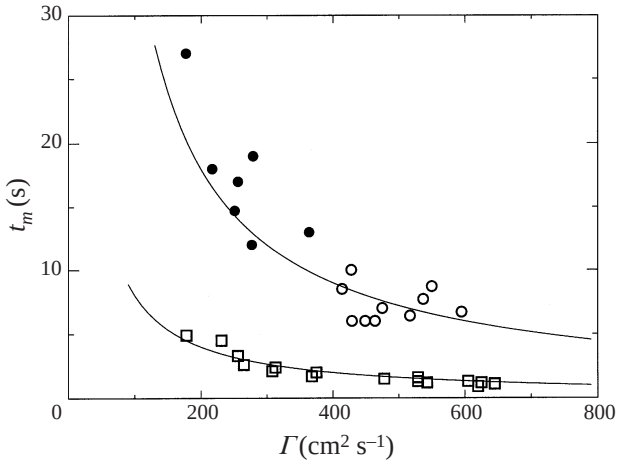

FIGURE 9. Dimensional merger time t_m as a function of the measured total circulation Γ: ○ 30% flap, observed; ●, 30% flap, estimated; □, 67% flap. The lines are $t_m = C_m\tau$ for each wing from figure 18(*a*).

of the lift distribution on the airfoil simply determine the circulations Γ_f and Γ_t. If, for example, the flow separates on the wing, the lift distribution, and the vortex strength ratio Γ_f/Γ_t change. At low chord Reynolds numbers Re_c, the flow separates at moderate angles of attack; hence, the lift distribution changes. The flow at low α is attached, and the flap vortex is stronger than the tip vortex. At high α the flow over the wing separates, resulting in a flap vortex which is weaker than the tip vortex (figure 8). The dynamics are determined by the ratio of their strengths. As long as the strength ratio is ascertained, the generation mechanism is not central to the discussion here.

Vortices in the wake exhibit little growth. The isovors in figure 5 of the vortex behind the simple wing show little growth during the run of the experiment. Some growth, however, appears to occur near the wing ($z/b < 5$). The single vortex following merger of two vortices shows a similar behaviour. This is partly visible in figure 6 where the tip and the flap vortices merge late in the flow. The behaviour is more clearly observed when the merger occurs closer to the wing at higher angles of attack. This behaviour is also observed behind the 30% flap airfoil. In general, the isovors show little growth beyond the immediate vicinity of the wing or the merger region. This poses a problem in that a vortex in a real fluid must grow. Experiments suggest that the vortex growth even at high Reynolds numbers shows a behaviour reminiscent of viscous diffusion (Jacob *et al*. 1997). Vortex growth is discussed further in the next section by examining the size of a vortex using a definition based on the velocity profile.

As seen in figures 7 and 8, when two corotating vortices are present, each vortex exhibits stretching as they coil around each other. Numerous *ridges* or *flutes* are present along the isovors. These ridges are repeatable and are not an artifact of the data processing. Another interesting observation is the breakup of the weaker vortex into filaments as it wraps around the stronger vortex.

When the vortices are shed from the airfoil, they are distinct. However, as the downstream distance increases, the vortices lose their identity and merge. In figure 7, merger occurs at $z/b = 40$ ($z/c = 240$) and in figure 8 at $z/b = 34$ ($z/c = 200$). The merger appears to be catastrophic. The wake continues to exhibit interesting

behaviour after the merger, namely the vortex system appears to forget the history of its formation. The emerging vortex becomes a straight rod and shows no obvious signs of its previous helical nature.

The dominant feature of the flow is the merger of the corotating vortices within one orbit period. Table 1 shows that the merger time t_m is shorter for the 67% flap airfoil than it is for the 30% flap airfoil. Another observation is that the merger time decreases with increasing towing speed and angle of attack, both of which increase Γ. Following this observation, t_m is plotted against Γ in figure 9, both measured quantities. The merger occurs much sooner for the smaller l; t_m decreases with increasing Γ. The scatter in the plot is a reflection of the uncertainties inherent in determining Γ and a somewhat subjective method of determining the merger time t_m. Data points for each wing suggest inverse power law fits that may be made congruent with a suitable scaling. The curves in the figures are $\sim 1/\Gamma$ which describe the trend well. The curves suggest the possibility of a rational scaling of the data which is presented below.

4. Analysis of results

4.1. *Vortex characterization*

Several integral quantities are calculated from the data and used in the discussion below. These quantities include the vorticity distribution and its first four moments, the centroid of vorticity, the vortex descent velocity, the kinetic energy, and the tensor of the vorticity distribution. The probability density function $p(\omega, t)$ is calculated for each flow as

$$p(\omega, t) = \frac{1}{A} \int_A \langle \mathrm{d}A \mid \omega \leqslant \omega' < \omega + \mathrm{d}\omega \rangle, \tag{4.1}$$

where $\mathrm{d}\omega$ is the bin size. During this calculation, the 73×53 domain (e.g. figure 4*b*, *c*) is cropped to 67×47 to remove spurious data. The bin size $\mathrm{d}\omega$ must be chosen on the order of or finer than the resolution of the ω calculations in aLPT to obtain statistics that are insensitive to data processing parameters. In these experiments, this corresponds to a number of vorticity bins on the order of a few hundred. The number of bins used here is 1000.

Vorticity behaves differently in two and three dimensions. The vortex stretching term $\boldsymbol{\omega} \cdot \nabla \boldsymbol{u}$ in the vector vorticity equation for incompressible flow allows for both vortex stretching and tilting in three dimensions, which can either intensify or weaken vorticity. Probability distribution functions of the components of the vorticity can shift to arbitrarily high values. The viscous diffusion term always smears the vorticity distribution, and hence arrests infinite intensification of vorticity. When the flow is confined to a plane in two dimensions, the vorticity is reduced to a single component ω which behaves as a passive scalar and intensification is no longer possible. Hence, in a two-dimensional viscous flow, the probability density function of vorticity $p(\omega, t)$ can shift only toward lower vorticity values. If the flow is also inviscid, then vorticity is convected with fluid elements and $p(\omega, t)$ remains unaltered. The behaviour of $p(\omega, t)$, therefore, can be taken as an indicator of two-dimensionality of the flow if it does not change significantly. On the other hand, substantial changes in $p(\omega, t)$ indicate three-dimensionality of the flow if viscous effects are negligible. In particular, $p(\omega, t)$ can be taken as a direct indicator of vortex stretching if a shift toward higher values of ω is observed. This is true even if the flow is viscous, since viscosity can only diffuse vorticity and shift $p(\omega)$ to lower values of ω, narrowing the distribution of $p(\omega)$. For

example, diffusing vorticity tends to homogenize ω, and hence, $p(\omega) \to \delta(\omega - \omega_0)$, where ω_0 is a constant. In addition, vortex stretching is the only mechanism of amplifying vorticity and is a three-dimensional event.

Moments of the axial vorticity distribution $\omega(x, y, t)$ are calculated as

$$\langle \omega^n(t) \rangle = \int \omega^n p(\omega, t)\, \mathrm{d}\omega. \tag{4.2}$$

The strength of the vortex $\Gamma(t)$ is determined as

$$\Gamma(t) = \langle \omega(t) \rangle A. \tag{4.3}$$

As a consequence of Helmholtz's laws, the statistics of the vorticity distribution of a patch of fluid particles remain invariant in an inviscid two-dimensional flow. If the boundaries of the domain of integration in equation (4.2) is chosen in regions where ω is negligible, then

$$\frac{\mathrm{d}\langle \omega^n(t) \rangle}{\mathrm{d}t} = 0, \tag{4.4}$$

even if the boundaries are fixed. Equation (4.4) is used below in the discussion of the behaviour of the corotating vortex pairs. The first four moments are, respectively, the mean, variance, skewness, and flatness of the distribution and are calculated for all the flows. These moments are scaled as $\langle \omega^n(t) \rangle / \omega_{ave}^n$ where ω_{ave} is the average vorticity in a suitably cropped region of the three-dimensional data $\omega(x, y, t)$.

The centre of a vortex $\boldsymbol{X}_c(t) = (X_c, Y_c)$ is determined by calculating its centroid using the vorticity field (e.g. figure 4*c*) as

$$\boldsymbol{X}_c(t) = \frac{1}{\Gamma(t)} \int \boldsymbol{x}\ \omega(\boldsymbol{x}, t)\, \mathrm{d}A. \tag{4.5}$$

The centroid is taken as a marker of the vortex trajectory. The vortex descent velocity $\boldsymbol{U}_c(t) = (U_c, V_c)$ is calculated by weighting the velocity field with the vorticity field as in Bilanin, Teske & Williamson (1977) and Marcus (1990):

$$\boldsymbol{U}(t)_c = \frac{1}{\Gamma(t)} \int \boldsymbol{u}(\boldsymbol{x}, t)\ \omega(\boldsymbol{x}, t)\ \mathrm{d}A. \tag{4.6}$$

The descent velocity of the centroid may also be interpreted as the velocity of the vorticity as a passive scalar if the flow can be considered two-dimensional. In that case, even if part of the vortex has already left the view of the camera, as is the case in figure 8, the calculation still correctly yields the velocity of the vortex if the vorticity distribution remains coherent. The asymptotic behaviour of $\boldsymbol{U}_c(t)$ is uniform due to the induced velocity of the counter-rotating vortex system. This limiting behaviour is used to infer the average counter-rotating vortex pair separation distance β

$$\beta = \frac{1}{2\pi}\ \frac{\langle \Gamma(t) \rangle}{\langle |\boldsymbol{U}_c(t)| \rangle}. \tag{4.7}$$

The above calculation presumes that the vortex pair may be approximated as a pair of line vortices. This approximation is deficient, though, on two counts: (i) the vortices are not infinitely long and (ii) they do not represent idealized line vortices which have infinite kinetic energy. The inaccuracy incurred due to this approximation, however, is comparable to experimental uncertainty in determining β. The velocity field of the vortex $\boldsymbol{u}_\Gamma(r, \theta, t) = (u_r, u_\theta)$ with respect to its centroid is defined as

$$\boldsymbol{u}_\Gamma(\boldsymbol{r}, t) = (u_r, u_\theta) = \boldsymbol{u}(\boldsymbol{x} - \boldsymbol{X}_c, t) - \boldsymbol{U}_c(t), \tag{4.8}$$

where $\boldsymbol{r} = \boldsymbol{x} - \boldsymbol{X}_c$. In equation (4.8), u_r and u_θ are the radial and azimuthal velocity components as measured in a cylindrical coordinate system attached to the centre of vorticity of the system.

The dimensionless kinetic energy $\mathscr{K}(t)$ of the vortex field is calculated from $\boldsymbol{u}_\Gamma(\boldsymbol{r}, t)$:

$$\mathscr{K}(t) = \frac{1}{\Gamma^2(t)} \int \tfrac{1}{2} \left|\boldsymbol{u}_\Gamma(\boldsymbol{r}, t)\right|^2 \mathrm{d}A. \tag{4.9}$$

The scaling is based on the fact that the induced downwash of the lifting vortex system on the wing transfers energy to the incoming fluid. This energy eventually ends up as the kinetic energy of the trailing vortex system which is used by Prandtl to estimate the vortex core size (see, for example, Saffman 1992). The same scaling can be deduced by simply using the facts that the induced drag of a finite wing is proportional to the square of the lift, and that the induced drag force essentially generates the work which is expended in the wake inviscidly. Thus, based on this argument, the dimensionless kinetic energy is expected to remain constant. This constant is $\pi/8$ for an isolated vortex (Saffman 1992, p. 103).

The moment-of-inertia tensor I_{ij} of the vorticity distribution is calculated with respect to the centroid as

$$I_{ij}(t) = \frac{1}{\Gamma(t)} \int (x_i - X_{c,i})(x_j - X_{c,j})\, \omega(\boldsymbol{x}, t) \mathrm{d}A. \tag{4.10}$$

This tensor is used to identify salient features of the vortex dynamics, such as the vortex size and core oscillations. In particular, $I_{ij}(t)$ is used to help identify the merger point of a pair of corotating vortices. The calculations of the tensor I_{ij} must be done with care, since even small values of ω at large distances from the centroid contribute substantially and may even eclipse the contribution from the centre of the vorticity.

4.2. *Vortex structure*

Figure 10 shows the structural data of a single vortex of flow 4 at $t = 6$ s (figure 5). The Reynolds number Γ/ν is about 2.4×10^4. The data are presented with respect to the centroid of the vortex, the location and velocity of which are determined from equations (4.5) and (4.6). Figure 10(*a*) shows a scatter plot of the azimuthal velocity distribution $u_\theta(r)$, where a linear inner core with a smooth transition to a potential vortex field is implied. The scatter increases at farther distances from the vortex core. The peak velocities are observed around $r/b \approx 0.1$. The figure is similar to figure 4(*b*) of Devenport *et al*. (1996) which is constructed from pointwise measurements and corrected for vortex wandering. The corresponding plot for vorticity distribution $\omega(r)$ is shown in figure 10(*b*) which is determined intrinsically by the velocity gradient tensor output of aLPT in equation (2.1). The vorticity is highest at the centre. It falls off rapidly and almost vanishes by $r/b \approx 0.12$. This implies that the vorticity is very compact and that the velocity spread in figure 10(*a*) at large distances from the core is due to irrotational motion of the flow field. The amplitude of the scatter at large r in figure 10(*a*) and 10(*b*) is indicative of the uncertainties in the measurements, while the scatter at the core of the vortex is a measure of the deviations from an axisymmetric state. This deviation will be more clearly observed in the structure of vortices prior to merger. The total circulation as a function of the radial distance from the centre of the vortex is calculated as $\Gamma(r) = \int \omega(r) \mathrm{d}A$ and is shown in figure 10(*c*). In this calculation, the area $A(r)$ is taken as a disk of radius r centred at $\boldsymbol{X}_c$. $\Gamma(r)$ monotonically approaches its asymptotic value of $\Gamma_o \approx 240$ cm^2 s^{-1} with no overshoot. The same qualitative behaviour of $\Gamma(r)$ is observed after merger of

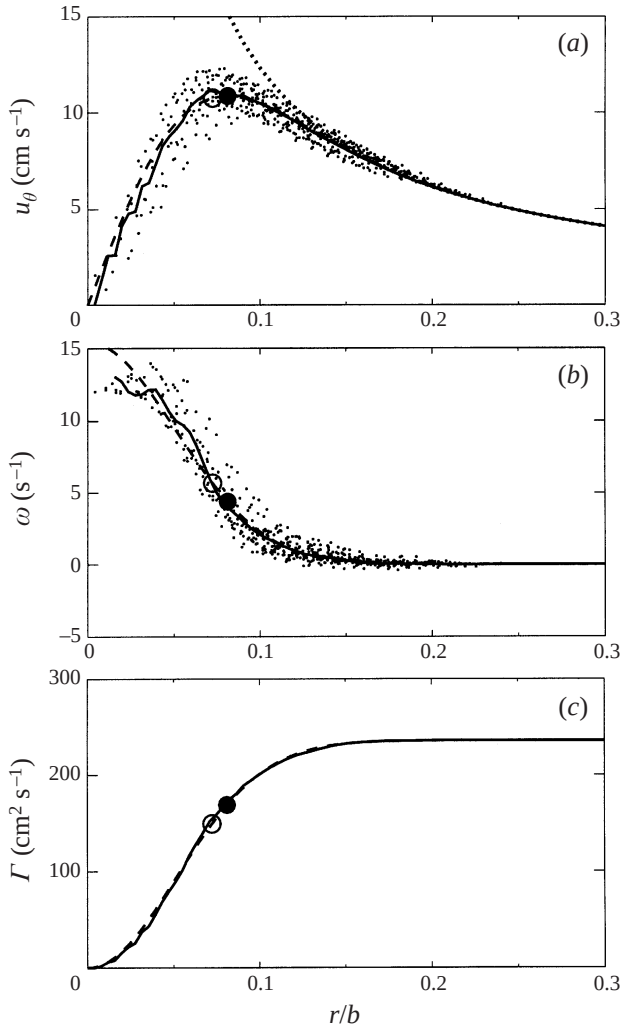

FIGURE 10. The structure of a single vortex, flow 4 at $t = 6$ s: (*a*) azimuthal velocity u_θ, (*b*) axial vorticity ω, and (*c*) circulation Γ as functions of the radial distance from the centre of a single vortex. The solid curve in (*a*) is $u_\theta = \Gamma(r)/2\pi r$ where $\Gamma(r)$ is from (*c*). The dotted curve in (*a*) is $u_\theta = \Gamma_o/2\pi r$ where $\Gamma_o \approx 240$ cm^2 s^{-1} is the average of the last quarter of $\Gamma(r)$ in (*c*). The solid curve in (*b*) is $\omega(r) = (\mathrm{d}\Gamma/\mathrm{d}r)/2\pi r$ calculated from the curve in (*c*) after some smoothing. The dashed lines in all figures correspond to a Lamb–Oseen vortex $\Gamma(r) = \Gamma_o(1 - \mathrm{e}^{-r^2/\sigma^2})$ with $\sigma = 0.073b$. Symbol ○ marks σ and ● the point of maximum u_θ at $r = 1.121\sigma$ ($r = 0.082b$).

the vortices in flow 39 which has the highest Reynolds number, about 6.4×10^4. A turbulent vortex, which is expected to occur at high Reynolds numbers, is thought to exhibit an overshoot of $\Gamma(r)$ (Govindaraju & Saffman 1971). The solid curve in figure 10(*a*) is $u_\theta = \Gamma(r)/2\pi r$ where $\Gamma(r)$ is taken from figure 10(*c*). The asymptotic dotted curve in figure 10(*a*) is $u_\theta = \Gamma_o/2\pi r$ and describes well the far-field velocity of the vortex. The solid curve in figure 10(*b*) is derived from the the $\Gamma(r)$ data in figure 10(*c*) as $\omega(r) = (1/2\pi r)(\mathrm{d}\Gamma/\mathrm{d}r)$. It is intended as a smooth curve fit to the data. The curve describes the far field well. The behaviour at the centre is perhaps an artifact of the measurement, for such details could not have survived this long in the flow.

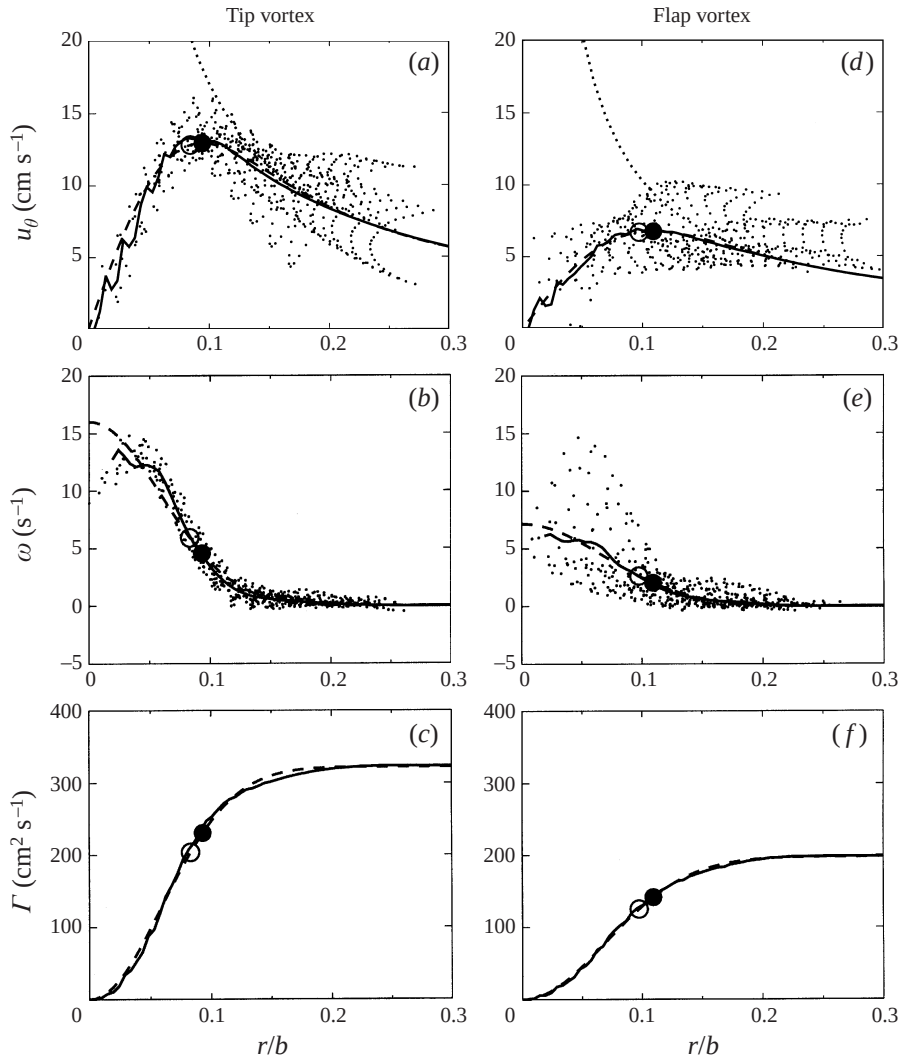

FIGURE 11. The structure of a vortex pair before merger, flow 16 at $t = 5$ s: left – tip vortex and right – flap vortex. The figure corresponds to the sample in figure 4. Symbols are the same as those in figure 10. (*a*),(*d*) azimuthal velocity $u_\theta(r)$, (*b*),(*e*) vorticity $\omega(r)$, and (*c*),(*f*) circulation $\Gamma(r)$.

Nevertheless, a core with almost uniform vorticity, hence near solid body rotation, is suggested in the figure.

The dashed curves in figure 10 represent a Lamb–Oseen vortex (Lamb 1932)

$$\Gamma(r) = \Gamma_o\left(1 - \mathrm{e}^{-r^2/\sigma^2}\right). \tag{4.11}$$

Its corresponding vorticity field is $\omega(r) = (\Gamma_o/\pi\sigma^2)\mathrm{e}^{-r^2/\sigma^2}$ and azimuthal velocity field is $u_\theta = (\Gamma_o/2\pi r)(1 - \mathrm{e}^{-r^2/\sigma^2})$. The parameters $(\Gamma_o, \sigma) = (238\ \mathrm{cm}^2\ \mathrm{s}^{-1},\ 0.073b)$ are determined from a least-squares curve fit to the data of figure 10(*c*). The circulation plot $\Gamma(r)$ is chosen as the starting point of curve fitting to the data, since it is an integral quantity that requires the minimum number of parameters. The parameter σ as well as the point of maximum azimuthal velocity $r_m = 1.121\sigma$ ($r_m = 0.082b$) are marked in figure 10. This r_m may also be used as a measure of the vortex core size,

which is smaller than $r_m = 0.11b$ predicted by Prandtl's arguments of conservation of kinetic energy (Saffman 1992). Despite the scatter in the data, this curve fit describes the general features of the vortex well. It overpredicts the vorticity at the core and the edges of the vortex and underpredicts in between. Nevertheless, both the curve fit in the figure and animation of the flows in table 1 indicate that the vortices remain compact and show little signs of growth. The values of σ/b for the duration of flow 4 hover around 0.07 with less than 4% growth. Similar growth trends are observable on isovors of all flows. This slow growth rate is reminiscent of slow viscous growth $\sim t^{1/2}$ as suggested by Moore & Saffman (1973), whose conclusion is further corroborated by Zeman (1995) and Jacob *et al*. (1997).

Figure 11 shows the structural data for the individual vortices of a corotating pair for flow 16 in table 1. The vortices are distinct at $t = 5$ s and permit individual analysis. The corresponding image, velocity field, and vorticity contours are shown in figure 4. In the figure, each vortex of the pair is treated singly as in figure 10. In contrast to the single vortex in figure 10, the plots of the azimuthal velocity show wide scatter at large distances from the centre of the vortices, which are marked in figure 4. This scatter is the result of the distorted shapes of the vortices, resulting from their interaction. The vorticity scatter plots show similar differences, but closer to the core where the scatter is wider than in figure 10(*b*) for a single wake vortex. In particular, the flap vortex has a concentration of points away from the centre which is due to the splitting visible both in the vorticity contour plot in figure 4(*c*) and the isovors in figure 7. These details are amplified further as the vortex pair undergoes severe structural changes ending in merger. The weaker flap vortex is distorted and eventually split. Therefore, a simple structural description of the vortices is inadequate. Nevertheless, figure 11 treats the vortices as axisymmetric to present features that may be compared to those in figure 10 for a single vortex. Interestingly, the circulation $\Gamma(r)$, an integral descriptor of the vortices, shows almost perfect Lamb–Oseen circulation distribution. The circulation profiles $\Gamma(r)$ for both vortices are shown in figure 11, along with the Lamb–Oseen vortex fit of equation (4.11). The curve fit parameters (Γ_o, σ) for the tip and the flap vortices are (325 cm^2 s^{-1}, 0.084*b*) and (197 cm^2 s^{-1}, 0.097*b*), respectively. The curve fits are remarkably close to the data. The corresponding velocity and vorticity profiles describe the average trends of the scatter plots well. Figures 10 and 11 indicate that the vortices tend to preserve a Lamb–Oseen structure with little or no appreciable growth.

The scheme of fitting the Lamb–Oseen structure to the average circulation distribution of a vortex is used to estimate the size of both the tip and the flap vortices, σ_t and σ_f, given in table 1. These estimates are based upon the structure of the vortices at early stages of the flows and may be used to ascertain the relative separation between them. The uncertainty is less that 10%. The data in the table suggest $\sigma \sim 2$ cm as a global measure of the vortex wake for the experiments here. This implies that $r_m/b \sim 0.07$, hence $0.1b$ may be taken as a measure of the vortex size here. Given that the vortex size behind a wing is determined by the spanwise lift distribution, $0.1b$ may be used beyond the experiments discussed here for comparison purposes. The observations suggest that these conclusions can be extended to the vortices of corotating pairs even though they are no longer axisymmetric. For stability analysis, however, fine details of the vortex structure must be considered.

4.3. *Onset of three-dimensionality and merger*

Figures 12–15 show the quantitative behaviour of the flows in figures 5–8 using the measures defined in equations (4.1)–(4.10). These include the vorticity density function

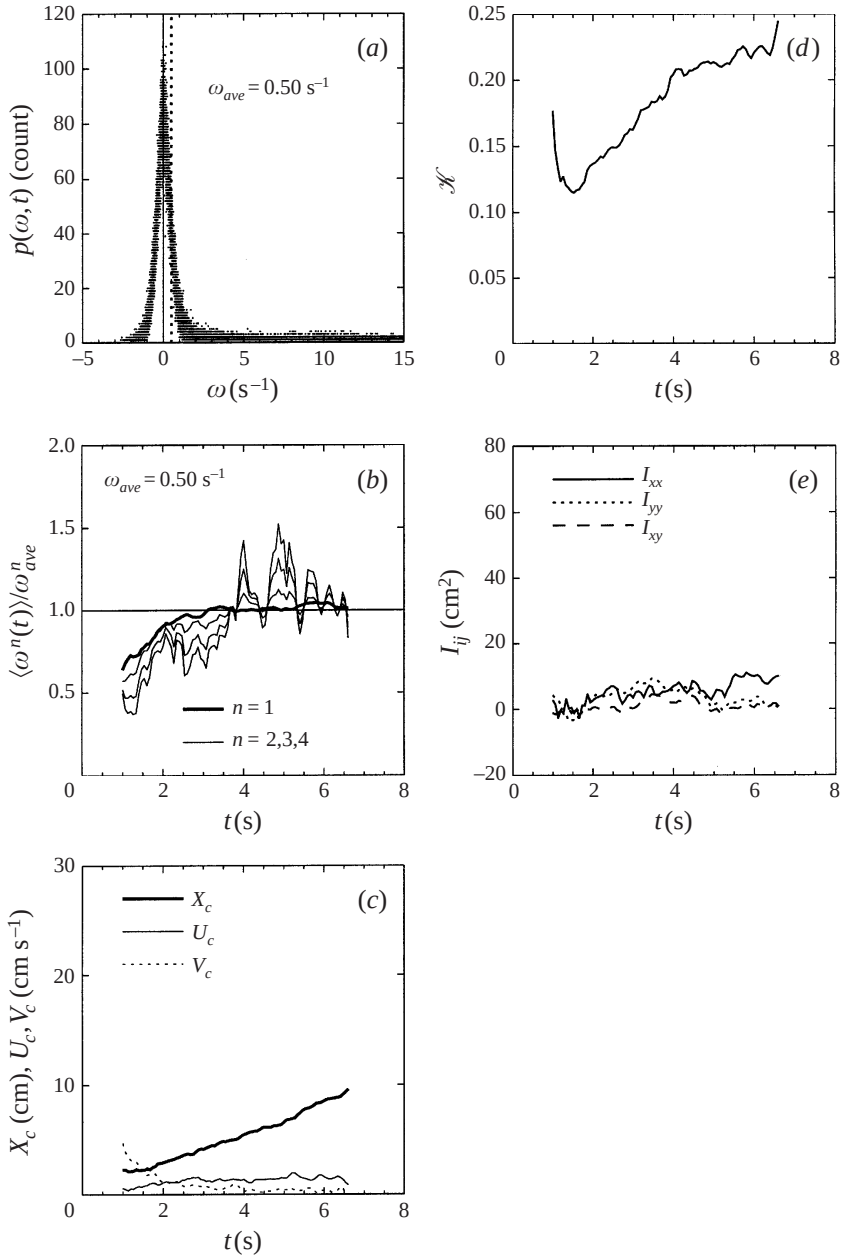

FIGURE 12. Flow 4 vortex characteristics. (*a*) Vorticity probability density function $p(\omega, t)$, the vertical dashed line marks the average vorticity ω_{ave} in measurement domain (x, y, t). (*b*) Moments of vorticity distribution $\langle\omega^n(t)\rangle$ $(n = 1, 2, 3, 4)$. (*c*) Position $X_c(t)$ and velocity $\boldsymbol{U}_c(t)$ of centroid of the vorticity distribution. (*d*) Kinetic energy $\mathscr{K}(t)$. (*e*) Vorticity distribution tensor $I_{ij}(t)$.

and its moments, the position and the velocity of centre of vorticity, the kinetic energy, and the vorticity distribution tensor for each flow.

The flow in figure 5 (flow 4) approximates the two-dimensional flow field of a single vortex with little growth. The p.d.f. $p(\omega, t)$ of vorticity is shown in figure 12(*a*) and its first four moments in figure 12(*b*). The p.d.f. does not significantly change

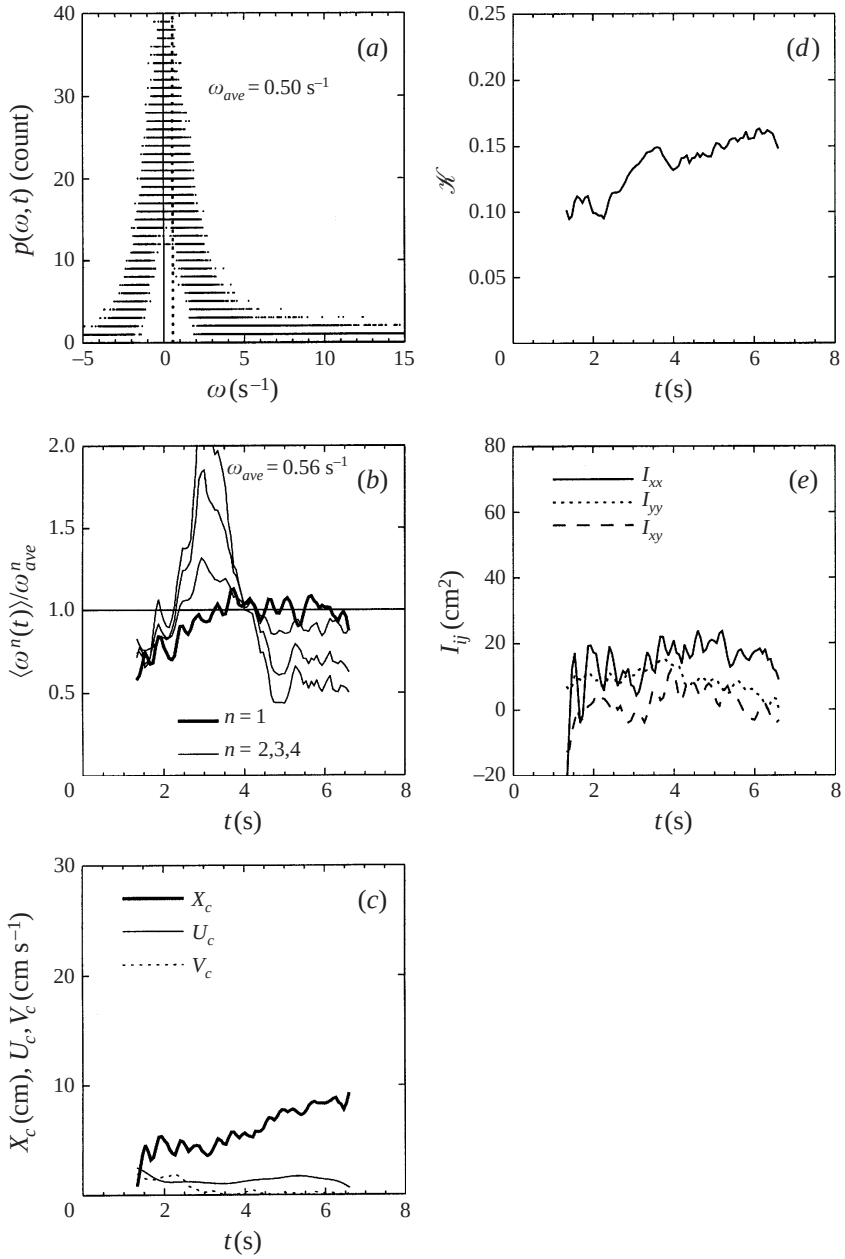

FIGURE 13. Flow 24 vortex characteristics. (*a*) Vorticity probability density function $p(\omega, t)$. (*b*) Moments of vorticity distribution $\langle \omega^n(t) \rangle$ ($n = 1, 2, 3, 4$). (*c*) Position $X_c(t)$ and velocity $\boldsymbol{U}_c(t)$ of centroid of the vorticity distribution. (*d*) Kinetic energy $\mathscr{K}(t)$. (*e*) Vorticity distribution tensor $I_{ij}(t)$.

during the evolution of the flow. The first moment of the p.d.f. $\langle \omega(t) \rangle$ indicates that the total circulation of the vortex is nearly constant. The global average vorticity ω_{ave} is marked as a vertical dashed line in figure 12(*a*). The second moment is also nearly constant until later in the flow. The third and fourth moments, however, show substantial activity, which points to the three-dimensional behaviour of even the simplest of the flows. The isovors in figure 5 suggest that short-wave instabilities

might exist in the vortex. No long-wave instabilities are apparent in the figure. The centroid of vorticity in figure 12(*c*) descends at a nearly constant velocity as expected of a pair of counter-rotating line vortices. After a period of increase, the kinetic energy of the vortex becomes constant at later times. The kinetic energy is infinite for a potential vortex. For the vortex of a rolled up sheet, however, it tends to a constant value, and the data in the figure support that trend. The domain of measurement is too small to capture all significant contributions to the energy integral, however, since figure 10 clearly indicate that the vortex possesses substantial kinetic energy at large distances. The vorticity inertia tensor $I_{ij}(t)$ in figure 12(*e*) shows fluctuations that are comparable in frequency to those seen in the higher moments of $p(\omega, t)$ in figure 10(*b*). The general trend of I_{ij} shows a slow growth.

The characteristics of flow 24 are shown in figure 13. In contrast to flow 4 in figure 12, the higher-order vorticity moment shows large fluctuations in figure 13(*b*). This is the clearest indication of the three-dimensionality of the vortex pair interaction. The sharp transition around $t = 4.5$ s nearly coincides with the beginning of merger of the isovors in figure 6. The merger time $t_m = 4.9$ s in table 1 nearly coincides with the minimum of the higher vorticity moments. The first moment of the p.d.f. remains nearly constant during the measurement period. Higher-order moments show some signs of oscillation before the merger. After the merger, however, they subside. A noteworthy observation in figure 13(*b*) is that the higher-order moments of vorticity decrease during and after the merger. This observation is discussed later. The motion of the centroid of the pair, however, seems to be unaffected by the details of the motion, i.e. it behaves as if it were a single vortex. The kinetic energy trend is similar to that in flow 4 and shows no indications of the merger. The inertia tensor I_{ij} shows, in addition to high-frequency oscillations, a one-cycle oscillation that ends when the merger is complete.

Flow 16 in figure 7 shows the vortex interaction at moderate Reynolds numbers. It is one of the most illustrative flows whose quantitative characteristics are shown in figure 14. The p.d.f. in figure 14(*a*) shows accentuated details. The low end of the p.d.f. remains unchanged, while the upper end shows details. The first moment of vorticity, and hence the combined strength of the vortex, is constant. No signs of the low-frequency oscillations are apparent. The second and third moments show strong time dependence and are nearly in phase. The fourth-order moment shows smaller amplitudes that are also in phase with the second and third moments. The oscillations begin prior to the merger of the vortices, subside during the merger, and resume after the merger. No evidence of these oscillations is apparent in the first moment of the p.d.f.

As remarked earlier for figure 13(*b*), all of the higher moments of the vorticity distribution show an abrupt decrease preceding the merger and remain low thereafter, while the first moment remains constant. The implication is that the spatial distribution of vorticity is shifting toward a uniform state. An alternative interpretation is that the vorticity is being mixed and becoming more homogenized. During the whole process, the centroid of the system continues as if it were a single vortex. Its trajectory is unaltered, though the descent velocity slightly decreases. Similarly, the kinetic energy in figure 14(*d*) shows no indications that a merger is occurring. The inertia tensor in figure 14(*e*) shows a very large-amplitude cycle which subsides as the merger is completed at $t_m \sim 8$ s.

Flow 23 in figure 8 shows the vortex interaction at moderate Reynolds numbers. Its characteristics are shown in figure 15. The flow is an example of the merger of two vortices of disparate size, where the stronger one overwhelms the dynamics of the

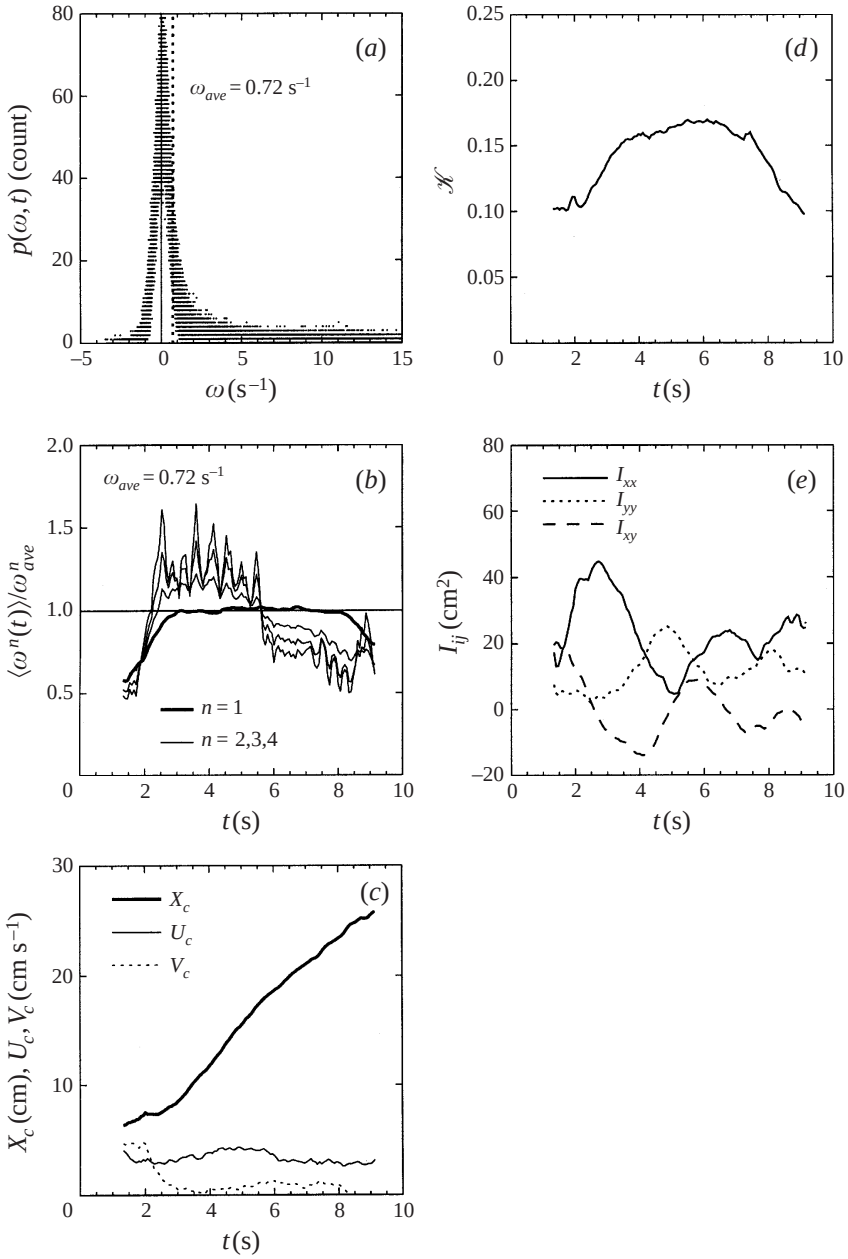

FIGURE 14. Flow 16 vortex characteristics. (*a*) Vorticity probability density function $p(\omega, t)$. (*b*) Moments of vorticity distribution $\langle \omega^n(t) \rangle$ ($n = 1, 2, 3, 4$). (*c*) Position $X_c(t)$ and velocity $\boldsymbol{U}_c(t)$ of centroid of the vorticity distribution. (*d*) Kinetic energy $\mathscr{K}(t)$. (*e*) Vorticity distribution tensor $I_{ij}(t)$.

pair. The p.d.f. in figure 15(*a*) shows pronounced signatures of the vortex interaction. Here again, the low end of the density function remains unchanged, while the high end shows pronounced variations in time. The total circulation remains constant. No clear signs of variation are apparent in the first moment of vorticity. The second and the third moments, however, show strong variations which are in phase. These oscillations seem to be briefly interrupted while the merger occurs at mid-point of

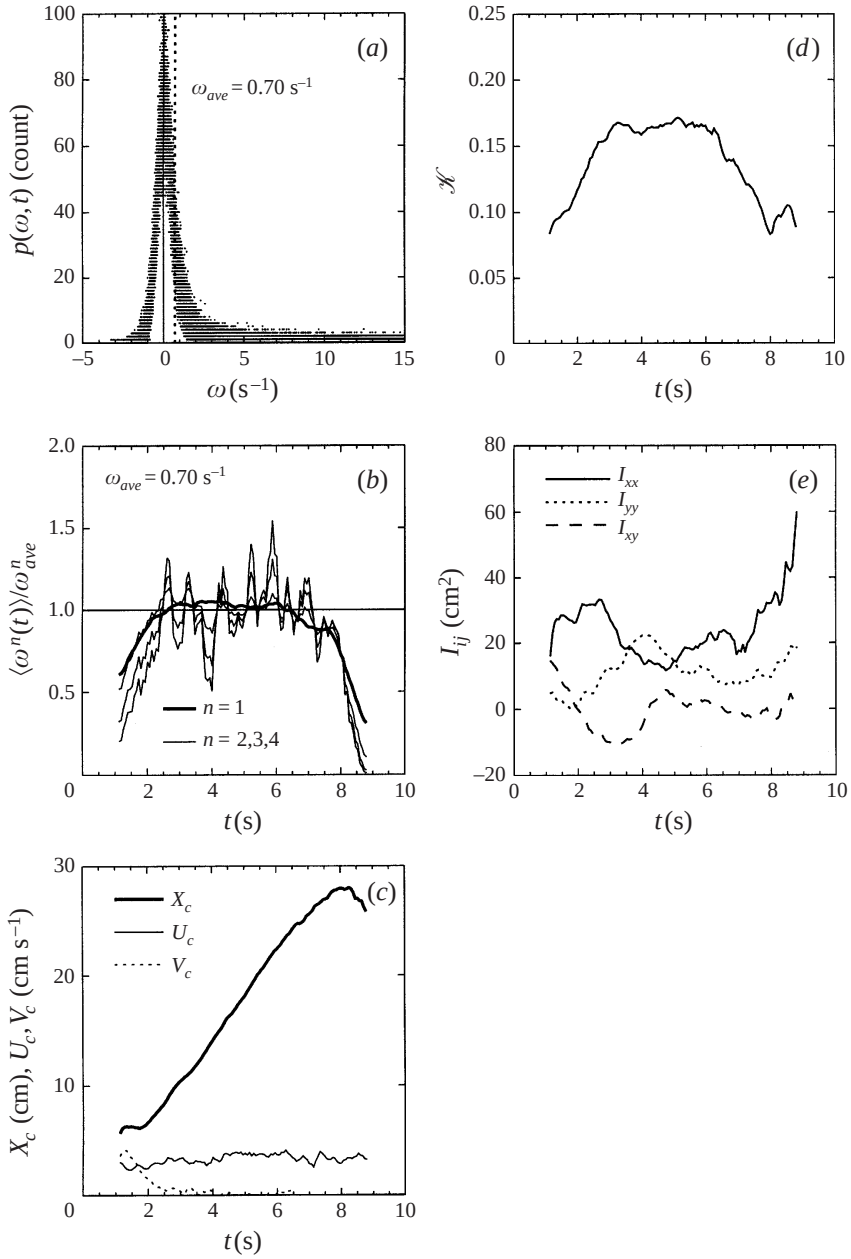

FIGURE 15. Flow 23 vortex characteristics. (*a*) Vorticity probability density function $p(\omega, t)$. (*b*) Moments of vorticity distribution $\langle\omega^n(t)\rangle$ $(n = 1, 2, 3, 4)$. (*c*) Position $X_c(t)$ and velocity $\boldsymbol{U}_c(t)$ of centroid of the vorticity distribution. (*d*) Kinetic energy $\mathscr{K}(t)$. (*e*) Vorticity distribution tensor $I_{ij}(t)$.

the data in figure 8. The isovors show a merger where the dominant vortex is hardly altered while the weaker one is shredded into filaments. The kinetic energy history does not suggest a dissipative event. The moment of inertia tensor I_{ij}, on the other hand, shows a high-amplitude cycle prior to merger and loses this feature after the merger.

Figure 16 shows the characteristics of individual vortices of flow 16 in figures 7

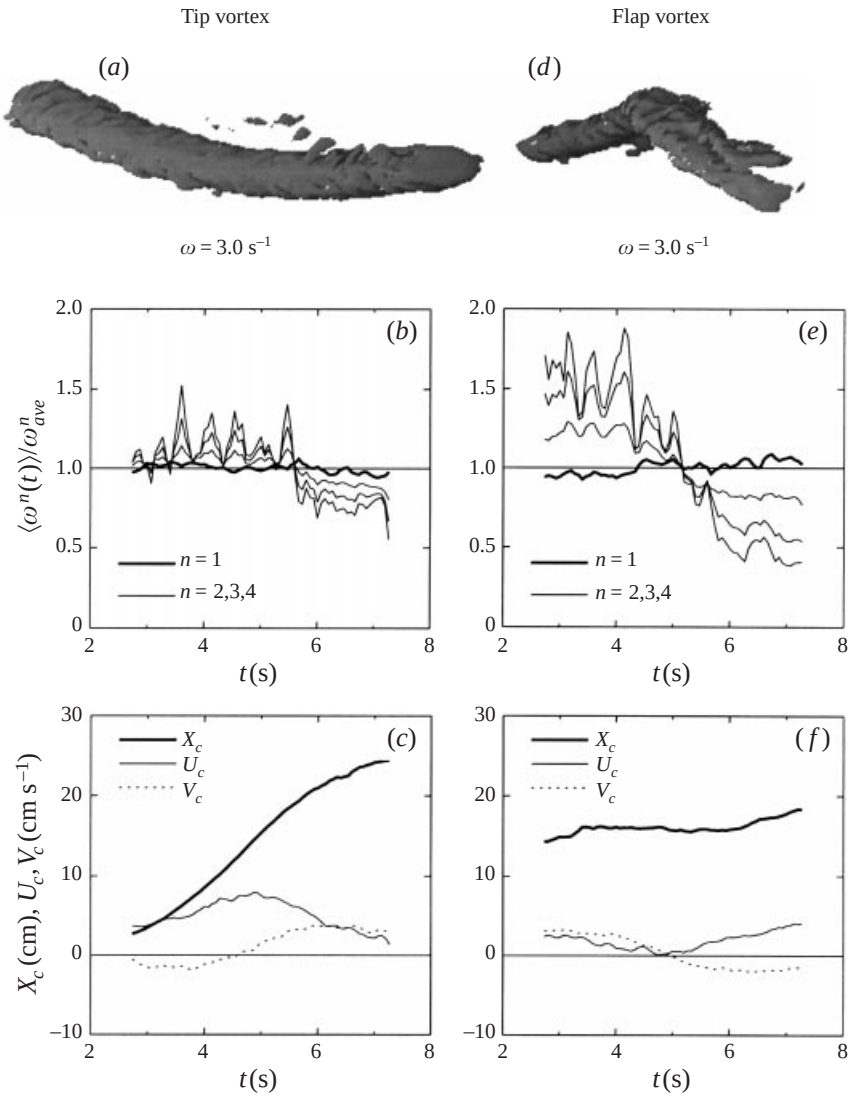

FIGURE 16. Characteristics of the individual vortices of flow 16. Left – tip vortex, right – flap vortex. (*a*),(*d*) isovors, (*b*),(*e*) vorticity moments $\langle\omega^n(t)\rangle$, and (*c*),(*f*) centroid characteristics.

and 14. The vortices are identified as *separate* when a sufficiently wide region of near-zero vorticity can be identified between them. The isovor segments are of the same duration, though they appear to have different lengths due to the particular perspective of their helices (cf. figure 7). The isovor of the tip vortex in (*a*) moves on a compact orbit and remains intact. The isovor for the flap vortex in (*d*), which is the weaker of the two, moves on a wider orbit, loses its circular shape, and splits into filaments about half way across the figure. The first moments of vorticity in (*b*) and (*c*) show that the vortices preserve their circulations before their merger. Their higher moments, however, show features much like the complete vortex system in figure 14(*b*). The oscillations of $\langle\omega(t)^n\rangle$ are much higher on the flap vortex, which is splitting. Further, the oscillation changes abruptly on the tip vortex but smoothly on the flap vortex during merger. As remarked earlier during the discussion of figures

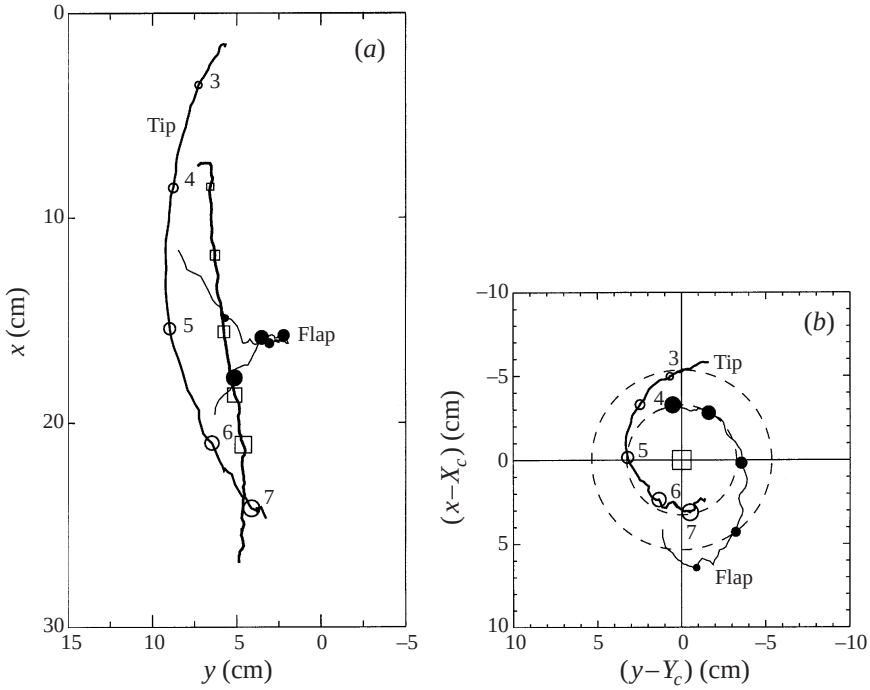

FIGURE 17. (*a*) Trajectories of the common centre of vorticity (□) and individual centres of vorticity of the vortices (○, tip vortex; ●, flap vortex) in the laboratory reference coordinates for flow 16 (figure 16). (*b*) Trajectories of the tip and flap vortices as observed from a coordinate system attached to the common centre of vorticity. The dashed circles correspond to two-dimensional vortex trajectories with $\Gamma_f/\Gamma_t = 0.61$ and separation of 8.6 cm. Numbers next to symbols indicate time in seconds. Symbol size increases with time.

13(*b*) and 14(*b*), individual vortices show a decrease in the higher moments of their vorticity distributions. This change is smaller for the stronger tip vortex than for the weaker flap vortex. This indicates that the homogenization is more severe for the weaker vortex than for the stronger one as observed on the isovors in figure 7. Further, the frequency of oscillations of the higher vorticity moments is lower on the individual vortices than on the pair in figure 14(*b*). This indicates that the vortices are undergoing instabilities at different frequencies and that measurements of the flow field of the pair show the combined signatures of the individual instabilities. Evidently, the merger is a three-dimensional event, and catastrophic for the weaker vortex. The centroid (*c*) and (*f*) data suggest cycloid paths which should be circular orbits when observed from the reference system of the centre of vorticity of the vortex pair. The tip vortex in figure 16(*c*) traces a sinuous trajectory, which is close to that of the centre of vorticity of the pair shown in figure 14(*c*). The flap vortex, being the weaker of the two, is hurled around the centre of vorticity of the joint system; hence its trajectory is substantially different than that of the joint system or of the tip vortex. The segment of its path captured in figure 14(*c*) corresponds to the part of its cycloid which forms a closed loop, hence looks nearly stationary from the laboratory reference frame.

Figure 17 shows the trajectories of the vortices of flow 16 in figure 14. Figure 17(*a*) shows, in the laboratory reference frame, the trajectory of the centre of vorticity of the pair shown in figure 14(*c*) and those of the individual vortices shown in figures

16(*c*) and 16(*f*). The common centre of vorticity descends uneventfully at a nearly constant velocity. The trajectories of individual vortices show orbital motion around the common centroid, which is reminiscent of cycloids. Near the wing, however, the tip vortex rises above the wing plane as observed both in experiments and calculations. The pair in figure 17 displays orbits much like the first cycle in the initial part of those shown in figure 3 of Bilanin *et al*. (1977). For real vortices which are bound at the wing, however, periodicity is not expected. In fact, the vortices merge by the time the first cycle is complete. In figure 17(*b*), the orbits are drawn as observed from $\boldsymbol{X}_c(t)$. The symbols marking the centres of the vortices and the centre of the vortex pair in figure 4(c) provide a snap shot of the orbits in the laboratory coordinate system ($t = 5$ s in figure 16). The two concentric circles are the trajectories of two-dimensional line vortices with a strength ratio of $\Gamma_f/\Gamma_t = 0.61$ and a separation of $(\beta/b)l = 8.6$ cm (table 1). The vortices spiral into their common centre. The event is three-dimensional. As the weaker vortex destabilizes and splits, it loses its coherence. As seen in figure 14, part of the disintegrating vortex moves into the centre, while part is thrown into the outer perimeter. This is a consequence of the invariants of vortex motion.

5. Vortex merger

5.1. *Merger mechanism*

The evidence in the isovors in figures 6–8, the data analysis in figures 13–15, and the detailed analysis in figures 16 and 17 show that the vortex merger is a three-dimensional inviscid phenomenon. Instabilities develop prior to merger and continue after it. During this interaction, the circulation of the vortex pair remains constant. Their common centroid moves uninterrupted. The kinetic energy of the measurement region shows no signs that a catastrophic event is taking place. The isovors show deformed and split vorticity surfaces and filaments. The cross-sectional areas of these filaments change in time, pointing to vortex stretching which is a three-dimensional event. The strength of a vortex remains constant, while the higher moments of its vorticity distribution show extreme fluctuations. Further, these moments decease during the merger, an indication that the vorticity is tending toward a more homogeneous distribution. No discernible signs of viscous effects are apparent. Based on these observations, we conclude that the vortex merger is a three-dimensional, inviscid event.

Figures 5–8 show that while no change is obvious in the behaviour of a single vortex over long periods of time (figure 5), the dynamics of two vortices has intriguing features (figures 6–8). One immediate observation is the onset of three-dimensionality, which seems to be intrinsic to the merger process. The best visual indicator of this is present on the isovors in figures 7 and 8. On high-vorticity isovors, vortex filaments that split off from the secondary vortex terminate in the data domain. This is clear evidence of vortex stretching (shrinking in this case) which can only take place in a three-dimensional flow field. Flow visualization experiments with strips of baked dye marking the boundary layers on the wing surfaces provided the first clues of these details, even though no quantitative results could be deduced. This is due to loss of traceability of the vorticity sheet when masked by the vorticity of the boundary layers on the wing surfaces. Velocity fields or streamline patterns such as those shown in figure 4 cannot yield these fine details, for they show integral behaviour of the flow field. Thus, an explanation of the merger mechanism may perhaps be better at the level of vorticity, a more primitive quantifier of the flow.

As an initial analysis, a two-dimensional model of the merger can be made which does not take into consideration vortex stretching. Consider the motion of two corotating vortices which are separated by l. Assume that the weaker vortex, which will experience higher straining, has a core size σ and is strained by the stronger vortex Γ_s. The strain rate e imposed on the weaker vortex is $e \sim \Gamma_s/2\pi l^2$ and, hence, the total extension rate ϵ of the vortex core is $\epsilon \sim \Gamma_s \sigma/2\pi l^2$. On the hypothesis that the merger begins when the total extension of the weaker vortex is comparable to their separation l, that is $\epsilon t_m \sim l$, the time to merger t_m can be determined as

$$t_m \sim \frac{2\pi l^2}{\Gamma_s} \frac{l}{\sigma}. \tag{5.1}$$

This estimate of the time to merger results in a value which is longer than the orbit period of the pair by a factor of at least l/σ. The factor l/σ is a measure of the initial vortex separation and implies that within this estimate, well separated vortices will take many orbit times to merge, if merger occurs at all. Two-dimensional numerical simulations indeed suggest this (Dritschel 1985, 1995).

Vortex merger occurs within one orbit time of the pair, and the result is catastrophic for the weaker vortex. This consistent observation suggests that the vortex merger is a three-dimensional event and cannot be explained by two-dimensional mechanics alone. Clearly, the definition of the time to merger depends on the merger criterion used. Visually, one can define an approximate time of merger as the point where one can no longer clearly identify separate vortices, using animation of the raw flow images and the vorticity field. This approach is subjective, yet unavoidable at times. A preferred method is to use quantifiable measures to determine the point of merger. For this purpose, the results in figures 12–15 are used. While several quantities remain unchanged or show little indication of merger, an estimate of the merger point (or the projected merger point) is made by collectively considering the evidence from direct observations of the raw flow images and vorticity animations along with the oscillations of the moments of the vorticity distribution, $I_{ij}(t)$. The first clear indication of interaction of the vortices is in the higher moments of the vorticity distribution. All high-order moments show oscillations that change their behaviour before and after the merger. Flow 16 is a noteworthy example. The p.d.f. moments in figure 14 exhibit persistent oscillations before any signs of interaction between the vortices. These oscillations dampen almost instantaneously preceding the visible signs of merger. After the merger is complete, the oscillations reappear. In this particular case, the time at which the oscillations reappear coincides with the visually identifiable merger point in figure 7. The vorticity distribution tensor $I_{ij}(t)$ provides additional features in identifying the merger point. When two distinct vortices are present, $I_{xx}(t)$ and I_{yy} are out of phase. However, when the vortices merge, these components become indistinguishable and seem to remain constant. The point of transition from one trend to the other may be identified as the merger point. Another key observation in identifying the point of merger is that when the merger occurs, the core of the dominant vortex stops orbiting and resumes a straight descent. This behaviour is visible in figures 6(*c*) and 8(*a*). In determining t_m listed in table 1, isovors similar to those in figures 6–8 are used as the primary source and corroborated results from the $I_{ij}(t)$ and $\langle \omega^n(t) \rangle$ histories. Once the merger time is determined, the location of the merger is determined from the $X_c(t)$ curve in figures 13(*c*)–15(*c*). The descent distances δ_m are also listed in table 1.

The dimensional merger time t_m was plotted in figure 9 and was discussed in some detail earlier. Motivated by observations that the merger occurs within one orbit time

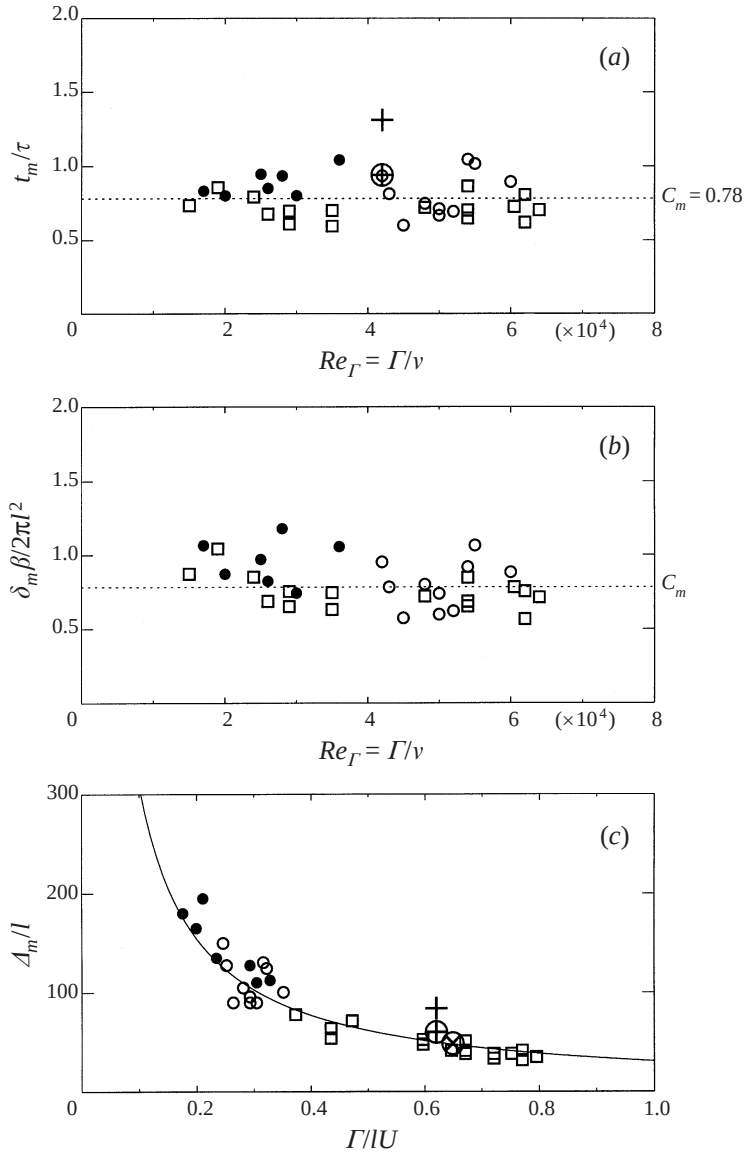

FIGURE 18. Dimensionless merger time and distance. (*a*) Merger time t_m, (*b*) descent to merger δ_m, and (*c*) distance to merger Δ_m as functions of the measured circulation Γ. ○, 30% flap; observed; ●, 30% flap, estimated; □, 67% flap; +, Vogel *et al.* (1996), stated; ⊕, Vogel *et al.* (1996), estimated; and ⊗, de Bruin et al. (1996), estimated form their Plot 2. Line in (*c*) is equation (5.10).

of the pair, t_m is scaled with the orbital period τ of the vortex pair

$$\tau = \frac{4\pi^2 l^2}{\Gamma}, \tag{5.2}$$

where the vortices are modelled as ideal line vortices, which are separated by a distance l and have a combined circulation of Γ (Lamb 1932). The dimensionless merger time t_m/τ is plotted against the measured total circulation Reynolds number $Re_\Gamma = \Gamma/\nu$ in figure 18(*a*). The flows where the merger occurs after the data acquisition period

are plotted as estimates based on the time taken for half an orbit. The figure confirms that merger occurs within one orbit time. The average merger time is on the order of τ,

$$t_m = C_m \tau, \tag{5.3}$$

with $C_m = 0.78$ as determined from the data in figure 18(*a*). No systematic dependence on Reynolds number is apparent. The flow studied by Vogel *et al*. (1996) is also shown in figure 18(*a*). Their stated merger point is at $(\Gamma/\nu, t_m/\tau) = (42\,000, 1.31)$, which is determined from turbulence measurements. Observing the hydrogen bubble markers indicated in their figure 2 at $x/c = 16$, a more comparable identification of the merger point is at $(\Gamma/\nu, t_m/\tau) = (42\,000, 0.94)$. Both estimates are shown in the figure. In either case, this independent observation supports the conclusion of figure 18(*a*). The curve fit implied in equation (5.3) is plotted as the two smooth curves in figure 9, where the appropriate values of l and Γ are used in the calculation of τ. The fitted curves describe the behaviour of $t_m(\Gamma)$ well. The deviation from the curves is due to uncertainties in determining the merger point rather than the robustness of scaling.

Since the centre of vorticity of the pair is observed to be translating nearly uniformly even when the vortices are separate, the descent distance to merger δ_m may be written as

$$\delta_m = \langle U_c \rangle \; t_m, \tag{5.4}$$

where $\langle U_c \rangle$ is determined from equation (4.6). Alternatively, δ_m can be determined from $\boldsymbol{X}_c(t)$ in equation (4.5) at $t = t_m$ as

$$\delta_m = |\boldsymbol{X}_c(t_m)|. \tag{5.5}$$

The distance δ_m can also be written as

$$\delta_m = C_m 2\pi \frac{l^2}{\beta}, \tag{5.6}$$

where equation (5.4) is used with $\langle U_c \rangle = \Gamma/2\pi\beta$. Figure 18(*b*) shows δ_m determined from equations (5.4) and (5.5) in the form suggested in equation (5.6). The constant of proportionality C_m defined in equation (5.3) represents well the average value of δ_m in part (*b*). As in part (*a*), no obvious dependence on the geometry or the vortex strengths Γ_i exists. The implication of equation (5.6) for a particular wing-flap geometry becomes clearer if δ_m is scaled with the wing span b

$$\frac{\delta_m}{b} = 2\pi \left(\frac{l}{b}\right)^2 \left(\frac{b}{\beta}\right). \tag{5.7}$$

For a given airfoil geometry b/β is a constant of order one ($4/\pi$ for an elliptically loaded wing, Saffman 1992). Equation (5.7) states that the descent distance to merger is a function of the wing geometry alone and is independent of the flow conditions within the assumptions of the discussion herein.

Based on these observations, a simple, inviscid model of the vortex merger in the wake of a lifting flapped wing can be proposed. The root circulation Γ of a wing of span b may be approximated as

$$\Gamma = \tfrac{1}{2} c_l U_\infty A/\beta, \tag{5.8}$$

where c_l is the wing lift coefficient and A the area. The orbit time τ can be expressed

in terms of c_l as

$$\tau = \frac{8\pi^2 \beta l^2}{c_l A} \frac{1}{U_\infty}. \tag{5.9}$$

The orbit time and, hence, the merger time inversely depends on the lift coefficient. At high lift configurations, such as take-offs and landings when the flaps are deployed, the merger times are shorter. The downstream distance $\Delta_m = U_\infty t_m$ required for the merger to occur can be expressed as

$$\frac{\Delta_m}{l} = C_m \frac{4\pi^2 l U_\infty}{\Gamma} \tag{5.10}$$

which is rewritten as

$$\frac{\Delta_m}{l} = \frac{8\pi^2}{c_l} \frac{\beta l}{A}. \tag{5.11}$$

The data from table 1 are shown in figure 18(c). The solid line in the figure is equation (5.10) which describes the data well. The flow studied by Vogel *et al*. (1995) falls close to the correlation suggested in figure 18(c). Also shown in the figure is one of the flows discussed by de Bruin *et al*. (1996). From their Plot 2, the flow parameters are estimated as $(\Gamma, l, U_\infty) = (14.5\ \mathrm{m^2\ s^{-1}}, 0.37\ \mathrm{m}, 60\ \mathrm{m\ s^{-1}})$ and is marked at $\Gamma / l U_\infty = 0.65$ ($Re_\Gamma \approx 10^6$). In the estimation of Γ, the incremental rotation in Plot 2 and equation (5.2) are used. The vortex pair should merge at $\Delta_m / l \approx 48$ (equation (5.10)) or at about 14 wing spans, which is much farther than the distance covered in their measurements.

5.2. *Vortex stretching*

The corotating vortices are initially distinct as the compact vorticity distributions in figures 10 and 11 indicate. As they rotate around their common centroid, the weaker vortex travels a greater distance and, thus, travels at a faster rate, which stretches the vortex tube. This stretching can be seen in figure 13 as the p.d.f. shifts toward higher vorticity values before merger occurs. The sudden increase in the higher moment of $p(\omega, t)$ in figure 13(b) is evidence of this stretching. Since the p.d.f. only shifts toward higher values of vorticity, little spreading or diffusion occurs in the vortices. An estimate of the relative stretching of the vortices may be made based on idealized helix lengths. Two vortices of strengths Γ_t and Γ_f at R_t and R_f from their common centroid orbit around the centroid at a period of

$$\tau = \frac{4\pi^2 (R_t + R_f)^2}{\Gamma_t + \Gamma_f}, \tag{5.12}$$

where the ratio of the orbital radii is $R_t / R_f = \Gamma_f / \Gamma_t$. If these orbits are stretched into the region behind the wing at the free-stream velocity U_∞, then the helices have pitch angles of

$$\gamma_{t,f} = \tan^{-1} \left(\frac{2\pi R_{t,f}}{\tau U_\infty} \right) \tag{5.13}$$

and lengths of

$$l_{t,f} = \tau U_\infty \left[1 + (\tan \gamma_{t,f})^2 \right]^{1/2}. \tag{5.14}$$

The differential stretching $\Delta l = l_t - l_f$ is, in view of small helix angles,

$$\frac{\Delta l}{\tau U_\infty} \approx \tfrac{1}{2}\Delta\gamma^2, \tag{5.15}$$

where $\Delta\gamma = \gamma_t - \gamma_f$. The differential stretching implied in equation (5.15) is too small to be the sole mechanism in the vortex merger. For example, $\gamma_{t,f} \sim 10^{-2}$ in figures 6 and 7. Hence, $\Delta l/\tau U_\infty \sim 10^{-4}$. This suggests that the three-dimensionality observed in these flows is brought about by a combination of the filament stretching and the development of vortex instabilities.

5.3. *Structure of merging vortex pair*

Figure 19 shows the streamline patterns at selected times for flow 16 in figure 7. The frames in figure 7(*a*) are drawn in the laboratory reference system and those in 7(*b*) in a coordinate system attached to the centre of vorticity of the vortex pair and rotating at the orbital angular velocity of $2\pi/\tau$. Note that the centre of vorticity of the system is descending at the velocity calculated in equation (4.6). The streamlines show nearly closed loops around the flap vortex. The outer streamlines spiral toward the stronger tip vortex, suggesting entrainment of fluid into the vortex system. These features are equally observable in the laboratory and the rotating reference system. The signature of the flap vortex in the rotating coordinate system, however, becomes less discernible. This is more clearly observable in the rotating reference frame at time 0.6τ. At the merger time of 0.8τ, the signs of entrainment have nearly vanished. The signature of the flap vortex continues to fade, though still identifiable even in the rotating reference system. At 1.0τ the vortices have lost their individual identities. In both reference systems, an elliptical streamline pattern has developed. No obvious signs of entrainment are present. Only a slight anomaly in the ellipse exists.

Figure 20 shows the structure of the merged vortex pair at $\tau = 1.0$ ($t = 8$ s) for flow 16. The scatter in the velocity plot in figure 20(*a*) is narrower than the scatter in either of the velocity plots for the tip and flap vortices in figures 11(*a*) and 11(*d*), respectively. This is an indication that the merged vortices are now behaving as a single vortex. The vorticity scatter plot in figure 20(*b*) still shows numerous bumps, indicating the existence of patches of vorticity in the flow field scattered around the perimeter. The circulation profile plot $\Gamma(r)$ in figure 20(*c*) of the merged vortex pair is showing noticeable differences from that of a Lamb–Oseen vortex (cf. figure 10*c*). The merged vortex has $\sigma = 0.18b$ while the tip and flap vortices had $\sigma = 0.084b$ and $\sigma = 0.093b$, respectively, as seen in figure 11.

As an example of a merged pair at a much later time, figure 21 shows the structure at $\tau = 4$ ($t = 3.3$ s) for flow 39 in table 1. The far field of the merged vortex seems to have settled. However, both the velocity and the vorticity plots show that the core of the vortex has asymmetries. The circulation plot in $\Gamma(r)$ in figure 21(*c*) shows that the Lamb–Oseen vortex fit is no longer as successful as it was earlier. This deviation may be due to the long lasting effects of the merger process which may have initiated structural changes.

5.4. *Additional factors in merger*

The vortex strength ratio Γ_f/Γ_t is an important factor in determining the details of the merger. The data in table 1 show the extent of available vortex strength ratios. These ratios are determined by isolating individual vortices in a plane using comparable windows. The uncertainty in the Γ_f/Γ_t estimates is less than 10% and typically 5%. The ratios in the flows range from 0.3 (flow 22) to 1.3 (flows 7, 31, and

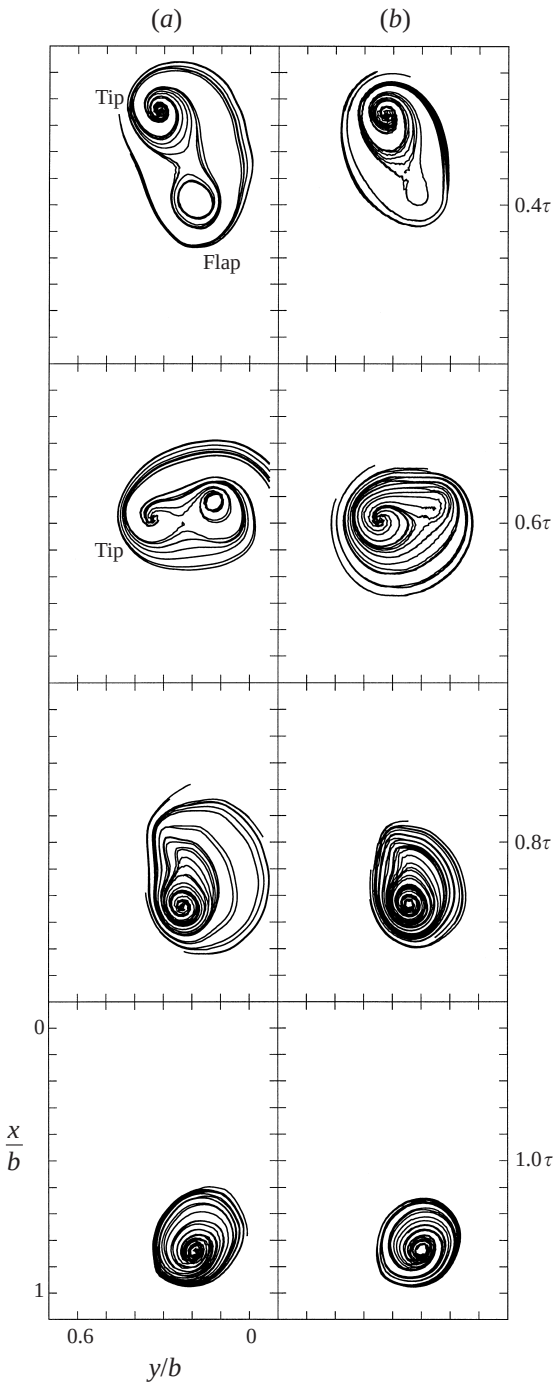

FIGURE 19. Selected streamline patterns for flow 16 (*a*) in laboratory reference frame and (*b*) in a reference frame rotating with the vortex pair. Time steps are marked in orbit period τ.

32), including a few near unity (flows 12, 13, and 24). When the vortices have different strengths, the stronger one dominates the dynamics of the interaction. The weaker one disintegrates around the stronger one. Merger is catastrophic and is complete within one orbit time. When one of the vortices is much weaker that the other (for

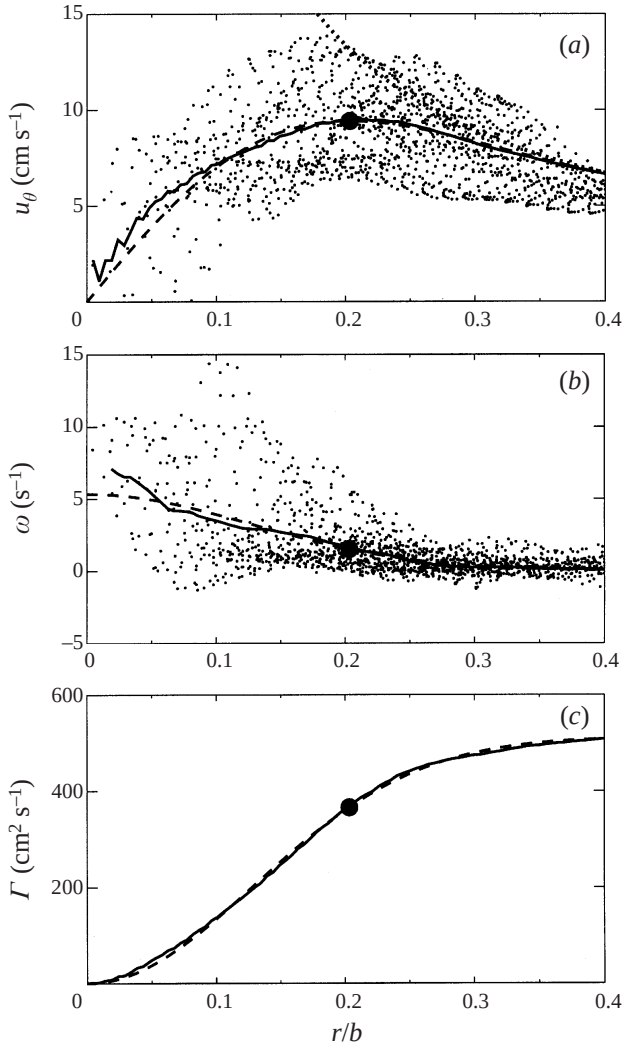

FIGURE 20. The structure of the merged vortex pair in flow 16 at $\tau = 1.0$ ($t = 8$ s): (*a*) azimuthal velocity u_θ, (*b*) axial vorticity ω, and (*c*) circulation Γ as functions of the radial distance from the centre of the vortex. The solid curve in (*a*) is $u_\theta = \Gamma(r)/2\pi r$ where $\Gamma(r)$ is from (*c*). The dotted curve in (*a*) is $u_\theta = \Gamma_o/2\pi r$ where Γ_o is the average of the last quarter of $\Gamma(r)$ in (*c*). The solid curve in (*b*) is $\omega(r) = (\mathrm{d}\Gamma/\mathrm{d}r)/2\pi r$ calculated from the curve in (*c*) after some smoothing. The dashed lines in all figures correspond to a Lamb–Oseen vortex $\Gamma(r) = \Gamma_o(1 - \mathrm{e}^{-r^2/\sigma^2})$ with $\sigma = 0.18b$. Symbol ● marks the point of maximum u_θ at $r = 1.121\sigma$ ($r = 0.20b$).

example, $\Gamma_f/\Gamma_t = 0.47$, flow 23 in figure 8), the weaker vortex is split rapidly axially and wrapped around the stronger vortex. The weaker vortex is torn into numerous spiral filaments along a cylindrical shell. If the vortices are of comparable strengths, the merger occurs more equitably. The stronger vortex maintains its integrity while the weaker one splits radially. The severity of this disintegration increases with increasing disparity. When the vortex strengths are nearly the same (flows 12, 13, and 24), their interaction shows marked differences from the others. The merger takes longer to complete. This is noticeable in figures 9 and 18. Also, the flow studied by Vogel *et al*. (1995) with $\Gamma_f/\Gamma_t = 1$ shows a longer merger time. The interaction of the vortices

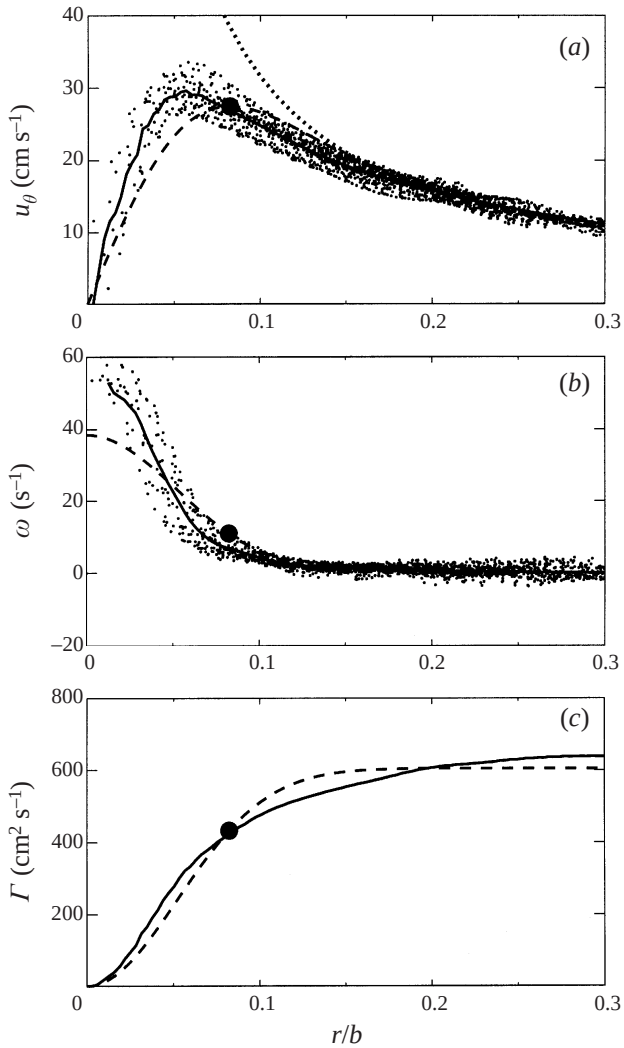

FIGURE 21. As figure 20 but for flow 39 at $\tau = 4.0$ ($t = 3.3$ s) with $\sigma = 0.074b$. Symbol ● marks the point of maximum u_θ at $r = 1.121\sigma$ ($r = 0.082b$).

basically takes place at the perimeter, where the vorticity is being homogenized. The higher-order vorticity moments indicate (not shown here) that this homogenization takes places gradually as opposed to the sudden onset observed in figure 14. Numerical simulations of two-dimensional vortex patches show similar behaviour when they are of equal strengths (Marcus 1990; Dritschel 1995). Further delineation of the effect of the strength ratio requires rigorous stability analysis and is beyond the scope of this paper.

Separation on the wing surface at high angles of attack directly affects the vortex behaviour in the wake by changing the strength of the flap and tip vortices. It also has an indirect effect on the vortices through the turbulence it creates in the wake of the wing. This effect combined with the fossil turbulence should be examined, especially when the turbulence intensity is high and the scales are right for an interaction. The effects are known to be rather dramatic. A further complication comes from

fluid stratification, which affects the behaviour strongly (Spalart 1998). A typical real vortex pair in an application is likely to have all of these extraneous effects present simultaneously. The present level of knowledge cannot predict the behaviour of vortices in such an environment.

6. Summary

The interaction of corotating vortex pairs in the wakes of flapped airfoils is studied experimentally at circulation Reynolds numbers ranging from 1.0×10^4 to 6.4×10^4. The parameters governing the vortex interaction are the vortex strengths Γ_t and Γ_f, the vortex separation l, and to a lesser degree the vortex sizes σ_t and σ_f. The vortex separation is determined by the flap geometry and only two values are available. By changing both the angle of attack and the towing speed, the vortex strengths are varied. The vortex sizes are less controllable. The distribution of vorticity off the wing determines the size of the vortices. Once formed, the vortices show little growth. A Lamb–Oseen vortex formulation is a good descriptor of single vortices, both differentially at the vorticity distribution level, and integrally at the circulation distribution level. For a pair of vortices, the Lamb–Oseen vortex remains a good integral descriptor of the circulation distribution of each vortex.

A pair of corotating vortices merge in approximately 0.8 orbit times. This time scale is insensitive to Re_Γ or the relative strength ratio Γ_f/Γ_t of the vortices. The orbit time also determines the scale of the events leading to merger of the vortices. For a typical wing–flap geometry producing a vortex pair, the orbital behaviour results in a merger distance that is much larger than the wing span. Since the vortex circulation, and hence the orbit time, scales with lift on the wing, the merger location occurs even farther downstream at low lift configurations. In the wake of a given wing, the distance that the vortices descend before merging depends on the geometry alone and is independent of the flow conditions. This observation, which is counter-intuitive, is a consequence of the fact that both the descent velocity and the orbital angular velocity scale with the circulation of the corotating vortex system. Hence, the descent distance to merger depends on the geometry of the lifting wing and is independent of the flow velocity and lift coefficient.

Measurements suggest that the merger mechanism is three-dimensional and inviscid. No evidence of viscous diffusion acting over the separation distance between the vortices is observed. Vortices are either wrapped around each other or shrink and spread over large regions around the dominant filament. The events leading to merger become discernible after about half of an orbit time. The first indication is a filamentation of the vortices. The details depend strongly on the relative strengths of the vortices. When the circulations of the vortices are comparable, both show signs of a radial filament formation. The inner filaments merge directly with the dominant vortex. The outer filaments shrink and spread their vorticity around the core. When one vortex is weaker, the breakup into filaments begins earlier along the axis. Leading filaments shrink, weakening vorticity, while trailing filaments merge with the dominant vortex. Vortex stretching accompanies stretching of the filaments prior to merger. If the smaller vortex is much weaker, it splits into many filaments. One or a few strong filaments fuse directly with the dominant vortex, while the remaining filaments are hurled into orbits at the fringes of the system. A decrease in the higher-order moments of the vorticity distribution during merger indicates that the merger tends to homogenize the vorticity distribution. The budgets for various vortex invariants are calculated and found to remain unaffected by the merger.

In view of the small helix angles when the vortices are orbiting around each other, one is inclined to invoke arguments from two-dimensional vortex dynamics to describe the behaviour of the pair. Two-dimensional vortex dynamics precludes vortex stretching, and, thus, cannot account for the observations discussed here. The merger of a corotating vortex pair within one orbit emphasizes that controlling the vortex wake behaviour by inciting instabilities in a system of multiple vortices (Crouch 1997) must be achieved within one orbit time, since excitation signatures may not survive their merger.

We thank R. L. Bristol, J. A. McCauley, J. M. Ortega, M. J. Sholl, and R. Spektor for their contributions to this work. We have benefited greatly from many discussions with Professor P. S. Marcus. This research was supported in part by the Boeing Commercial Aircraft Group (Contract 322648-07LLN) and NASA (Grant NAG-1-1816).

REFERENCES

AGARD 1996 *The Characterization and Modification of Wakes from Lifting Vehicles in Fluids Trondheim, Norway, May 20-23, 1996. NATO-AGARD CP*-584.

BAKER, G. R., BARKER, S. J., BOFAH, K. K. & SAFFMAN, P. G. 1974 Laser anemometer measurements of trailing vortices in water. *J. Fluid Mech.* **65**, 325–336.

BALSER, M., MCNARY, C. A. & NAGY A. E. 1974 Acoustic backscatter radar system for tracking aircraft trailing vortices. *J. Aircraft* **11**, 556–562.

BILANIN, A. J., TESKE, M. E. & WILLIAMSON, G. G. 1977 Vortex interactions and decay in aircraft wakes. *AIAA J.* **15**, 250–260.

BRUIN, A. C. DE., HEGEN, S. H., ROHNE, P. B. & SPALART, P. R. 1996 Flow field survey in trailing vortex system behind a civil aircraft model at high lift. *NATO-AGARD CP* 584, pp. 25.1–12.

CHEN, A. L., JACOB, J. D. & SAVAŞ, Ö. 1997 Isovors: vortex wake flows catalog. *Research Rept.* UCB-ITS-RR-97-3. Institute of Transportation Studies, University of California at Berkeley.

CROOM, D. R. 1976 The development and use of spoilers as vortex attenuators. In *Symp. on Wake Vortex Minimization* (ed. A. Gessow), NASA-SP-4096.

CROUCH, J. D. 1997 Instability and transient growth of two trailing-vortex pairs. *J. Fluid Mech.* **350**, 311–330.

CROW, S. C. 1970 Stability theory for a pair of trailing vortices. *AIAA J.* **8**, 2172–2179.

DEVENPORT, W. J., RIFE, M. C., LIAPIS, S. I. & FOLLIN, G. J. 1996 The structure and development of a wing-tip vortex. *J. Fluid Mech.* **312**, 67–106.

DRITSCHEL, D. G. 1985 The stability and energetics of corotating uniform vortices. *J. Fluid Mech.* **157**, 95–134.

DRITSCHEL, D. G. 1995 A general theory for two-dimensional vortex interactions. *J. Fluid Mech.* **293**, 269–303.

FAA 1991 *FAA International Wake Vortex Symposium. DOT/FAA/SD*/92-1.

GARODZ, L. & CLAWSON, K. 1993 Vortex wake characteristics of B757-200 and B767-200 the tower fly-by technique. *NOAA-TM-ERL-ARL*-199-V1.

GESSOW, A. (Ed.) 1976 *Symposium on Wake Vortex Minimization*, *NASA-SP*-4096.

GOVINDARAJU, S. P. & SAFFMAN, P. G. 1971 Flow in a turbulent trailing vortex. *Phys. Fluids* **14**, 2074–2080.

GREENE, G. C. 1986 An approximate model of vortex decay in the atmosphere. *J. Aircraft* **23**, 566–573.

HALL, M. G. 1972 Vortex breakdown. *Ann. Rev. Fluid Mech.* **4**, 775–802.

HALLOCK, J. N. 1991*a* Aircraft Wake Vortices: An Assessment of the Current Situation. U.S. Department of Transportation, *DOT-FAA-RD* 90-20, *DOT-VNTSC-FAA-90-6.*

HALLOCK, J. N. 1991*b* Aircraft Wake Vortices: An Annotated Bibliography (1923-1990). U.S. Department of Transportation, *DOT-FAA-RD-90-30, DOT-VNTSC-FAA-90-7.*

HALLOCK, J. N. 1997 Wake Vortex Bibliography. http://www.volpe.dot.gov/wv/wv-bib.html.

Hinton, D. A. (1996) An aircraft vortex spacing system (AVOSS) for dynamical wake vortex spacing criteria. *NATO-AGARD CP*-584, paper 23.

Jacob, J., Liepmann, D. & Savaş, Ö. 1996 Natural and forced growth characteristics of the vortex wake of a rectangular airfoil. *NATO-AGARD CP*-584, pp. 27.1–12.

Jacob, J., Savaş, Ö. & Liepmann, D. 1997 Trailing vortex wake growth characteristics of a high aspect ratio rectangular airfoil. *AIAA J.* **35**, 275–280.

Kopp, F. 1994 Doppler lidar investigation of wake vortex transport between closely space parallel runways. *AIAA J.* **32**, 805–810.

Lamb, H. 1932 *Hydrodynamics*. Cambridge University Press.

Lanchester, F. W. 1908 *Aerodynamics*. D. Van Nostrand.

Marcus, P.S. 1990 Vortex dynamics in a shearing zonal flow. *J. Fluid Mech.* **215**, 393–430.

Maxworthy, T. 1972 The structure and stability of vortex rings. *J. Fluid Mech.* **15**, 15–32.

Moore, D. W. & Saffman, P. G. 1973 Axial flow in laminar trailing vortices. *Proc. R. Soc. Lond.* A **333**, 491–508.

Moore, D. W. & Saffman, P. G. 1975 The instability of a straight vortex filament in a strain field. *Proc. R. Soc. Lond.* A **346**, 413–425.

Olsen, J. H., Goldberg, A. & Rogers, M. (Eds.) 1971 *Aircraft Wake Turbulence and its Detection*. Plenum Press.

Rossow, V. J., Fong, R. K., Wright, M. S. & Bisbee, L. S. 1995 Vortex wakes of two subsonic transports as measured in 80- by 120-foot wind tunnel. *AIAA 13th Applied Aerodynamics Conf. Proc.*, Paper 95-1900.

Saffman, P. G. 1992 *Vortex Dynamics*. Cambridge University Press.

Sholl, M. J. & Savaş, Ö. 1997 A Lagrangian parcel tracking method for velocity measurements in high-gradient flows. *Phys. Fluids* (submitted). Also, *AIAA Paper* 97-0493.

Spalart, P. R. 1998 Airplane trailing vortices. *Ann. Rev. Fluid Mech.* **30**, 107–138.

Spreiter, J. R. & Sacks, A. H. 1951 The rolling up of the trailing vortex sheet and its effect on the downwash behind wings. *J. Aero. Sci.* **18**, 21–32.

Tsai, C.-Y. & Widnall, S. E. 1976 The stability of short-waves on a straight vortex filament in a weak externally imposed strain field. *J. Fluid Mech.* **73**, 721–733.

Vogel, C. M., Devenport, W. J. & Zsoldos, J. S. 1995 Turbulence structure of a pair of merging tip vortices. In *Tenth Symp. Turb. Shear Flows, Penn. State U., University Park, PA, August 14–16, 1995*.

Zeman, O. 1995 The persistence of trailing vortices: a modeling study. Structure of turbulent line vortices. *Phys. Fluids* **7**, 135–143.